

1 ECMWF TECHNICAL MEMORANDUM**2 Can global rainfall forecasts identify areas at risk of flash floods? Proof of
3 concept for Ecuador**

4 Fatima M. Pillosu^{1,2}, Agathe Bucherie³, Carolynne Hultquist⁶, Andrew Kruczakiewicz^{3,4,5}, Calum Baugh², Humberto
5 Vergara^{7,8}, Thomas Haiden², Florian Pappenberger², Elisabeth Stephens^{1,4,9}, Christel Prudhomme^{2,10,11}, Hannah L.
6 Cloke^{1,9,12,13}

7 ¹ Department of Geography and Environmental Science, University of Reading, Reading, UK

8 ² Forecast Department, European Centre for Medium-range Weather Forecasts, Reading, UK

9 ³ International Research Institute for Climate and Society (IRI), Columbia Climate School, New York, USA

10 ⁴ Red Cross Red Crescent Climate Centre, The Hague, The Netherlands

11 ⁵ Faculty of Geo-Information Science and Earth Observation, University of Twente, Enschede, The Netherlands

12 ⁶ Center for International Earth Science Information Network (CIESIN), Columbia Climate School, New York, USA

13 ⁷ Cooperative Institute for Mesoscale Meteorological Studies (CIMMS), The University of Oklahoma, Norman, OK

14 ⁸ NOAA National Severe Storms Laboratory (NSSL), Norman, OK

15 ⁹ Department of Meteorology, University of Reading, Reading, UK

16 ¹⁰ Department of Geography and Environment, University of Loughborough, Loughborough, UK

17 ¹¹ UK Centre for Ecology and Hydrology, Wallingford, United Kingdom

18 ¹² Department of Earth Sciences, Air, Water and Landscape Science, Uppsala University, Sweden

19 ¹³ Centre of Natural Hazards and Disaster Science, CNDS, Sweden

20 **Correspondence:** Fatima M. Pillosu (fatima.pillosu@ecmwf.int)

21 **Abstract.** Globally, flash floods are one of the costliest natural hazards for property damage and loss of life. The low accuracy
22 of flash flood forecasts beyond a few hours limits their use in early warning systems. This study assesses the performance
23 of ECMWF ensemble forecasts (ENS) and ecPoint rainfall forecasts in the identification of areas at risk of flash floods up to
24 medium-range lead times. A one-year objective verification analysis was conducted for flash flood event in Ecuador. The
25 varied climate and the presence of a comprehensive flood report database made it an attractive site for verification. The
26 verification results suggest that ecPoint outperforms ENS in areas where rainfall originates from small-scale convective
27 systems. Where rainfall originates from large-scale convective systems, ecPoint and ENS performances are comparable,
28 except for a better identification of the actual magnitude of the rainfall events. The latter outcome is paradigm-shifting as
29 assesses that, under certain weather conditions, raw global NWP rainfall forecasts can be used to predict areas at risk of
30 flash floods with global coverage and up to medium-range leads. This study also proposes a methodology that uses short-
31 term ecPoint-Rainfall forecasts as a proxy for point rainfall observations to define the magnitude of flash-flood-triggering
32 rainfall thresholds to be used in the objective verification. Due to the probabilistic nature of the ecPoint output, this
33 approach allows to simulate a very high-density observational network and provide the needed rainfall thresholds also in
34 data-scarce regions.

35 **Plain language summary.**

36 **Word count.** 9545 words, excluding abstract, tables, captions, and references.

37 **Keywords.** Ensemble rainfall forecasts, ecPoint, flash flood forecasting, flash flood observations, Ecuador.

40 1 Introduction

41 Flash floods cause large societal, economic, and environmental impacts (Jonkman and Vrijling 2008; Dordevic et al.
42 2020). They can happen due to prolonged rainfall or extreme rainfall over a short-term period, leading to a sudden rise of
43 river water levels or the inundation of low-lying areas (Zanchetta and Coulibaly 2020; Speight et al. 2021). In Latin America,
44 flash flood impacts are exacerbated by rapid, unregulated urbanization of floodplains, human-induced catchment
45 degradation, high poverty levels, lack of preparedness plans, and inadequate infrastructure (Pinos and Quesada-Román
46 2022). For example, flash floods in Ecuador are the deadliest form of flooding, and some long-term impacts include
47 infrastructure damage, agricultural losses, business and education interruptions, health service disruptions, and
48 waterborne disease outbreaks (Galarza-Villamar et al. 2018). Approximately 60% of all floods in Ecuador are flash floods
49 (Kruczkiewicz et al. 2021a), and their frequency is expected to increase due to climate change (Hirabayashi et al. 2021). This
50 study aims to enhance preparedness and mitigation strategies against this escalating threat, particularly in regions with
51 limited resources and data, by assessing the effectiveness of global rainfall forecasts in identifying areas at risk of flash
52 floods.

Forecast-triggered mitigation strategies, such as early warning systems (Šakić Troglić et al. 2022; Coughlan de Perez et al. 2022) and forecast-based financing protocols (De Perez et al. 2016; Bischiniotis et al. 2019), have shown to improve resilience, decrease mortality, and lower recovery costs against riverine floods. Yet, they hinge on accurate, timely predictions. In lower-income countries, accurate forecasts with even longer lead times are required to set cost-effective mitigation strategies (Bazo et al. 2019; Kiptum et al. 2023). Over the years, flash flood forecasting systems have been developed at local/regional (Speight et al. 2018; Corral et al. 2019; Ibarreche et al. 2020; Ramos Filho et al. 2021; Shuo et al. 2021), national (Javelle et al. 2016; Liu et al. 2018), and continental scale (Raynaud et al. 2015; Gourley et al. 2017), with different degrees of model complexity and forecast accuracy. Due to large uncertainties in their forecasting chain, flash floods are more difficult to predict than riverine floods (Zanchetta and Coulibaly 2020; Speight et al. 2021). Poor historical data on flash flood occurrence and impact (Lowrie et al. 2022), inaccurate predictions of extreme localised rainfall (Zeman et al. 2021), and challenging representation of detailed hydrological processes dependent on topography, soil conditions, and terrain coverage that modulate flash flood occurrence and severity (Xing et al. 2019) limit the predictability of flash floods. Thus, forecast-triggered mitigation strategies have been limited for flash floods (De Perez et al. 2016).

Several studies have found that low-complexity, index-based systems using key predictors like rainfall and soil moisture can offer more accurate flash flood predictions than more complex, physically-based models, especially in larger domain systems (Alfieri and Thielen 2015; Hurford et al. 2012; Raynaud et al. 2015; Ma et al. 2021; Zanchetta et al. 2022; Luong et al. 2021). However, the prevailing belief that high-density observational networks (Javelle et al. 2010) or km-scale rainfall forecasts (Davolio et al. 2017; Song et al. 2019) are needed to represent the features of flash-flood-triggering rainfall events has limited the development of a flash flood forecasting system that provides medium-range forecasts over a continuous global domain. Radar-derived rainfall predictions extend only a few hours ahead (Imhoff et al. 2022) and the skill of km-scale rainfall forecasts decreases significantly after day 2 lead time (Barrett et al. 2019). Furthermore, their spatial coverage is patchy. Due to the limitations outlined above, the Flash Flood Guidance System with Global Coverage is not developed over a continuous global domain but is built instead on a patchwork of systems over multiple locations (Georgakakos et al. 2021). Consequently, many areas of the world still remain without access to flash flood guidance, highlighting the need for alternative approaches to address the challenge of providing medium-range flash flood predictions over a continuous global domain.

Global Numerical Weather Prediction (NWP) models, such as the ECMWF's Integrated Forecasting System, are increasingly seen as a viable solution to this challenge. These models provide daily global rainfall predictions up to medium-range leads but have historically struggled to accurately predict extreme localized rainfall events due to their coarse resolution and parametrization schemes (Emerton et al. 2016; Wen et al. 2021). Owing to recent improvements in global NWP forecast accuracy (Lavers et al. 2021; Haiden et al. 2023), the interest in using them to provide flash flood guidance in data-scarce regions and extend predictions' lead times has recently increased (Bucherie et al. 2022b). In addition, the development of the ecPoint statistical post-processing technique has improved the representation of the features of flash-flood-triggering rainfall events by transforming global grid-based forecasts into probabilistic point-scale predictions and improving the reliability and discrimination ability of the ECMWF's ensemble (ENS) rainfall forecasts up to day 10, especially for extremes (Hewson and Pillosu 2021).

Since there remains a significant gap in leveraging global rainfall NWP forecasts for flash flood forecasting, this study aims to bridge this gap by evaluating and comparing the performance of ENS and ecPoint rainfall forecasts in identifying areas at risk of flash floods. Ecuador, with its extensive flash flood database and high susceptibility to flash flooding, serves as an ideal test bed for this research (Kruckiewicz et al. 2021b). Two research questions are posed in this study. Can short-range ecPoint rainfall forecasts be used as proxies for in-situ rainfall observations in data-scarce regions to establish rainfall thresholds for an objective flash flood verification analysis? How well do ENS and ecPoint rainfall forecasts identify areas at risk of flash floods? The innovation of this research is threefold. First, it provides a complete objective verification analysis of forecasting systems, including estimates of forecast reliability and discrimination ability, to provide a nuanced assessment of the systems' performance. Second, rainfall forecasts are assessed against rainfall observations, and their suitability for flash flood prediction is simply assumed (Hewson and Pillosu 2021; Gascón et al. 2023). The objective verification in this study is conducted using historical flash flood reports in recognition of the non-linear relationship between flash floods and triggering rainfall events. Third, it proposes using short-range ecPoint rainfall forecasts as proxies for in-situ observations in data-scarce regions to calculate the flash-flood-triggering rainfall thresholds to be used in objective verification.

This paper is organized as follows. Section 2 provides background information on Ecuador's geography and rainfall/flood climatology. Sections 3 and 4 describe the data and methods used in the verification analysis. Section 5 presents the results of the objective verification analysis, while section 6 presents results from a case-study-based subjective verification analysis. Section 7 discusses the verification results, and section 8 draws the concluding remarks for the study.

2 Background: geography, rainfall climatology and flooding in Ecuador

Located in north-western South America, Ecuador includes continental Ecuador and the Galápagos Islands in the Pacific Ocean, 1000 km from the mainland (inset in **Figure 1a**). The Andes run north to south through Ecuador (**Figure 1a**) and split

it into three main regions (Vuille et al. 2000): "La Costa", which comprises the Andes' western slopes and the coastal plains along the Pacific Ocean; "El Oriente", which covers a plateau containing 2% of the Amazon basin and the eastern slopes; and "La Sierra", which contains the inter-Andean region between the western and eastern slopes of the Andes. This study considers only the continental landmass, hereafter referred to as "Ecuador". The domain of interest, including the borders with Colombia, Peru, and the Pacific Ocean, contains a total of 1090 grid boxes. This general domain is then split into the three main regions mentioned above using Ecuador's topography in the ENS grid (see **Figure 1b**). Grid boxes below 600 m above sea level and to the west and the east of the longitude 78.2 °W belong to "La Costa" (i.e., 321 grid boxes) and "El Oriente" (299 grid boxes). Grid boxes above 600 m were assigned to "La Sierra" region (470 grid boxes).

The rainy season in "La Costa" spans from December to May (Illibay-Yupa et al. 2021). Broad-scale atmospheric and oceanic phenomena modulate the intensity and spatial variability of rainfall. The extreme phases of El Niño Southern Oscillation, known as El Niño (i.e., above-average sea surface temperature in the Pacific Ocean) and La Niña (i.e., below-average), enhanced and decreased the average rainfall during the rainy season, respectively (Recalde-Coronel et al. 2014; Tobar and Wyseure 2018). In addition, certain phases of the Madden-Julian Oscillation, 1 and 8 (i.e., when a convection centre is over the Western Hemisphere and Africa) and 4 and 5 (i.e., when a convection centre is over the Maritime continent), are associated with an enhancement and decrease in precipitation, respectively (Recalde-Coronel et al. 2020). "La Sierra" has two main rainy seasons (i.e., February-May and October-November). Precipitation spatial patterns in the inter-Andean valleys are more complex than in "La Costa" because rainfall is typically generated by smaller-scale convective systems (Vuille et al. 2000). Additionally, as air masses lose much of their humidity on both flanks of the Andes, precipitation amounts in "la Sierra" are relatively lower than those in the other two regions, varying between 800 and 1500 mm/year (Vuille et al. 2000; Buytaert et al. 2006). Several studies (Buytaert et al. 2006; Bendix et al. 2006; Junquas et al. 2022) have shown that in the Andean region, most of the rainfall occurs during the daytime, particularly in the afternoon hours, between 2 pm and 7 pm local time (LT). It rains throughout the year in "El Oriente", with the wettest (driest) months being April-July (September-October). Rainfall climatology in "El Oriente" is primarily influenced by strong convective activity across the Amazon Forest and water vapor variations from the sea surface temperature of the tropical Atlantic Ocean (Vuille et al. 2000).

Floods can cause considerable material loss and deaths in "La Costa" and "La Sierra" because they are heavily populated and contain Ecuador's two most important industrial areas, Guayaquil in Guayas and Quito in Pichincha (**Figure 1c**). Prolonged rainfall events in "La Costa" can generate extensive, severe surface runoff far from rivers and cause rivers to flood vast plain areas (Galarza-Villamar et al. 2018). Intense shorter-lived rainfall events (i.e., less than one day) can also cause severe, sudden surface runoff (Galarza-Villamar et al. 2018). Rivers in "La Sierra" are susceptible to extreme localised rainfall events and, consequently, are prone to flash flooding (Laraque et al. 2009; Pinos and Timbe 2020). The river flows in "El Oriente" show a much stronger response to seasonal rainfall than a single rainfall event because of the size and length of Amazonian rivers, floodplain storage, and shallow riverbeds (Trigg et al. 2009).

3 Data

3.1 Flash flood reports

Disaggregation by flood type and specific documentation about historical flash flood events and their impacts are rare in many regions of the world, primarily due to a lack of commonly accepted flash flood definitions (Kruczakiewicz et al. 2021a; Bucherie et al. 2022a). Kruczakiewicz et al. (2021b) developed a method to assign an "Enhanced Flash Flood Confidence Index (EFFCI)" for flood events in historical flood datasets, based on text mining of disaster reports and a flash flood susceptibility index extracted from the geophysical properties of the location of the events. The EFFCI is an estimate of the likelihood of a flood event being a flash flood, ranging from 1 (not very likely) to 10 (extremely likely). The flash flood database in Ecuador was mainly compiled from two datasets, DesInventar (UNDRR 2021) and the Ecuadorian Secretariat for Disaster Management (SNGRE), and it contains 4967 flood events from 2007 to 2020. In addition to the EFFCI index, most entries in the flash flood database contain information about the location (with latitude and longitude coordinates) and the day and time (in local time) of flood occurrence. As a result of applying this method to Ecuador, a historical dataset of flood occurrences and impacts is available, with specific information on the likelihood of events being flash floods (Bucherie et al. 2021). Although this dataset is the best attempt to address historical flash floods in Ecuador, it is essential to note that it is based on disaster reporting processes carried out on the ground and not systematically collected over time. Consequently, it can present gaps, inconsistent descriptions of flood processes over time, and uncertainty in geolocation.

This study considered flood reports from 2019 to define the climatology of rainfall events associated with flash floods. Events from 2020 were used to perform an objective verification analysis. Three EFFCI thresholds were considered to evaluate the impact of uncertainty around a flood report as a flash flood event: $\text{EFFCI} \geq 1$ (all flood reports), $\text{EFFCI} \geq 6$ (flood reports that are likely to be flash floods), and $\text{EFFCI} \geq 10$ (flood reports that are highly likely to be flash floods). **Figure 2** shows the spatial distribution of such flood reports. **Figure 3** shows the time distribution of flash flood reports with $\text{EFFCI} \geq 6$.

166 3.2 Rainfall observations

167 Rainfall observations from the SYNOP network transmitted by the Global Telecommunication System (GTS) were used
 168 in this study to represent Ecuador's rainfall climatology and provide a context for both the estimated rainfall totals
 169 associated with flash flood events and the objective verification results. In the ECMWF's internal database, only 12-hourly
 170 rainfall observations with accumulation periods ending at 00 and 12 UTC, between the 1st of January 2010 and the 31st of
 171 December 2020, are available for Ecuador. **Figure 4a** shows their spatial distribution, while **Figure 4b** shows their temporal
 172 distribution. Not all days have observations. "El Oriente" has only one observation in a given day, while most of the days in
 173 "La Costa" and "La Sierra" have 4 to 8 observations in a given day, with peaks of 10 observations in "La Costa" and 14 in "La
 174 Sierra". **Figure 4c** shows the average rainfall over the entire study period for each accumulation period. The sinusoidal
 175 pattern in all three regions confirms what was reported in Section 2 regarding the diurnal cycle of marked rainfall in Ecuador.
 176 From the available observations, "La Costa" is the region with the most marked rainfall diurnal cycle with peak at night-
 177 time (i.e., accumulation period ending at 12 UTC) of ~3.5 mm/12h and throughs at daytime (i.e., accumulation period ending
 178 at 00 UTC) of ~1 mm/12h, and an average rainfall overall of ~2.2 mm/12h. "La Sierra" shows instead a very small diurnal
 179 cycle with an amplitude of just ~0.1 mm/12h between night-time and daytime rain, and an average of 1.6 mm/12h. It also
 180 appears that the times at which peaks and troughs occur are inverted to those in "La Costa". Although the spatial coverage
 181 of the rainfall observations in "El Oriente" is very poor, it is possible to observe that the average rainfall in the rain forest is
 182 substantially bigger than in the other two regions (i.e., ~4.8 mm/12h) and that the amplitude of the rainfall's diurnal cycle
 183 is ~1 mm/12h. **Figure 4d** shows the distribution of the rainfall totals on a given day for each accumulation period. More
 184 than 50% of the observations were less than 1 mm. "La Costa" is the region that has more frequent observations above 100
 185 mm/12h in the accumulation period ending at 12 UTC, which corresponds to the local night-time. During daytime rain (i.e.,
 186 accumulation period ending at 00 UTC) in "La Costa", and in both accumulation periods in "La Sierra" is rare to observe any
 187 rainfall >=100 mm/12h. However, it is possible to observe two extreme rainfall observations in the accumulation period
 188 ending at 00 UTC in "La Sierra" of up to ~260 and 400 mm/12h.

189 3.3 Rainfall forecasts: ECMWF ENS and ecPoint

190 The ECMWF ENS consists of one control run starting from the best possible representation of unperturbed initial
 191 conditions, and 50 perturbed members starting from perturbed initial conditions (using singular vectors and a data
 192 assimilation ensemble) and stochastic model uncertainties(Buizza 2019). Up to day 15, ENS forecasts were saved in the
 193 native octahedral reduced-Gaussian with a resolution of ~18 km at the equator (Owens & Hewson, 2018). Over the period
 194 used to compute the climatology of rainfall events associated with flash flood events (1st January to 31st December 2019)
 195 and the verification period (1st January to 31st December 2020), three different model versions were run operationally at
 196 ECMWF: 45r1¹ (for forecasts from 1st January to 10th June 2019), 46r1² (from 11th June 2019 to 12th July 2020), and 47r1³
 197 (from 13th July to 31st December 2020). The mismatch of the model versions over the periods considered in this study is
 198 unlikely to adversely affect the verification results because no significant changes were made in the physics of the rain
 199 generation mechanisms.

200 ecPoint is a decision-tree-based statistical post-processing technique that transforms global grid-based forecasts into
 201 probabilistic point-scale forecasts (Hewson and Pillosu 2021). The post-processing technique aims to provide forecasts that
 202 mirror observations from rain gauges by addressing the two main factors affecting the performance of the global NWP
 203 model output against point verification: systematic biases (Lavers *et al.*, 2021) and lack of information on forecast sub-grid
 204 variability (Göber *et al.*, 2008). For each raw ENS member, ecPoint generates an ensemble of 100 point-rainfall values based
 205 on the error distributions between forecasts and observations that vary according to different weather scenarios at the
 206 grid-box level. For example, when on a grid box, the model mainly predicts large-scale rainfall with light winds, the raw
 207 model output tends to be representative of point rainfall totals within that grid box, and ecPoint generates an ensemble
 208 with a smaller spread compared to the case of mainly convective rainfall with light winds. In the latter case, zero rainfall
 209 would be expected at many points and very large rainfall amounts at a few points. From the current operational
 210 configuration of ENS forecasts (i.e., 51 ensemble members), the 5100 point-scale rainfall values were distilled in percentiles
 211 from the 1st to 99th. ecPoint forecasts are provided in the same native grid of ENS forecasts up to day 10 lead times and in
 212 four overlapping 12-hourly accumulation periods with valid times starting at 0, 6, 12, and 18 UTC.

213 **Figure 5** shows examples of the ENS and ecPoint rainfall forecasts from the 85th and 99th percentiles. Typically,
 214 percentiles from ecPoint lower than or equal to the 85th percentile (**Figure 5c**) have lower rainfall forecast values than the
 215 ENS (**Figure 5a**). This is because, generally, the number of zero rainfall totals is larger in ecPoint than in ENS. This is a bias
 216 correction applied to the rainfall forecasts by ecPoint, as ENS tends to overpredict small rainfall totals(Haiden *et al.* 2023).
 217 On the contrary, big percentiles (typically above the 90th percentile) tend to show larger rainfall totals on ecPoint than in
 218 ENS. This can be noticed in **Figure 5d** by the overall domination of the orange colour (i.e., rainfall totals between 50 and 80
 219 mm/12h) compared to **Figure 5b** where the dominant colour is green (i.e., rainfall totals between 10 and 30 mm/12h). It

¹ www.ecmwf.int/en/forecasts/documentation-and-support/evolution-ifs/cycles/summary-cycle-45r1

² www.ecmwf.int/en/forecasts/about-our-forecasts/evolution-ifs/cycles/summary-cycle-46r1

³ www.ecmwf.int/en/forecasts/about-our-forecasts/evolution-ifs/cycles/summary-cycle-47r1

is noteworthy that ecPoint does not always increase the amounts of the rainfall forecasts. In “La Costa”, the rainfall totals in ecPoint are lower than those in ENS. This is because the post-processing considered that the raw rainfall forecasts might be overpredicted under the predicted grid-box weather type. While Hewson and Pillosu (2021) showed with a global objective verification analysis over a one-year period that, up to medium-range lead times (i.e., day 10 forecasts), ecPoint provides forecasts for point-scale rainfall with better reliability and discrimination ability than ENS, especially for extremes, it is interesting to compare how ENS and ecPoint perform in the prediction of rainfall in Ecuador. **Figure 6a** and **Figure 6b** shows 2020’s 12-hourly rainfall average from SYNOP observations (in grey) and forecasts (ENS in red and ecPoint in blue), respectively, for “La Costa” and “La Sierra”. There is no degradation in performance with lead times up to day 10, and both forecasting systems reproduce the fact that Ecuador’s rainfall is affected by a diurnal cycle. However, neither ENS nor ecPoint can correctly represent the peaks and troughs of the diurnal cycle of rainfall. While in “La Costa” ENS represents exceptionally well the rainfall peaks during nighttime, it significantly overestimates the rainfall over daytime (**Figure 6a**). With the aim of reducing the daytime bias, ecPoint unnecessarily reduces the nighttime rainfall and reduces the overall amplitude of the rainfall’s diurnal cycle. This is because for 12-hourly rainfall, ecPoint makes no distinction between rainfall at different times of the day. **Figure 6c** shows how ENS predicts most of the rainfall during nighttime on the western slopes of the Andes, while ecPoint tends to remove most of the rainfall, leaving the rainfall in the Pacific coast mostly unchanged (**Figure 6e**). During the daytime, the ENS still produces high amounts of rainfall, primarily on the western slopes of the Andes (**Figure 6d**). ecPoint applies a general reduction in rainfall in “La Costa” (**Figure 6f**). It can be observed that ecPoint’s overall rainfall average (blue dashed line in) is closer than that of ENS (red dashed line) to the observed average (grey dashed line). In “La Sierra” (**Figure 6b**), although again ecPoint’s overall rainfall average is closer than ENS to the observed average, both forecasts significantly overestimate the absolute values of daytime and nighttime rainfall and the amplitude of the observed rainfall diurnal cycle. In **Figure 6c** to **Figure 6f**, it can be observed that ecPoint applies a reduction in the rainfall forecasts generalized over the entire region.

4 Methods

The two main attributes of any probabilistic forecasting system are reliability and discrimination ability, which together determine the performance of the system (Jolliffe and Stephenson 2011). Reliability and discrimination ability are defined for events exceeding a certain rainfall threshold (e.g., 50 mm/12h). Hereafter, this rainfall threshold will be referred to as verifying rainfall threshold (VRT). Reliability measures whether the chosen VRT is predicted with a probability that equals the average frequency at which such an event is observed. Discrimination measures the ability of the forecasting system to distinguish situations that lead to events exceeding the VRT or not.

This study faced two main challenges. Since they were not known a priori, the first challenge was to define the magnitude (in mm) of the flash-flood-triggering rainfall events to be used as the VRTs in the objective verification analysis. Section 4.1 describes in detail the method used to define the VRTs and the pink area in the flowchart in **Figure 7** provides a graphical representation of the steps described in section 4.1. The second challenge relates to the objective verification analysis. First, due to the intrinsic characteristics of the observational dataset, it was not possible to define univocally observational yes- and no-events. Second, since the probabilistic rainfall forecasts were converted into binary forecasts (yes- or no-event), reliability in the usual probabilistic sense cannot be computed. The frequency bias was then calculated to determine the overall reliability of the system, indicating whether the system is, on average, under- or over-forecasting the occurrence of flash flood events. Sections 4.2.2 and 4.2.1 describe in detail the assumptions adopted to carry out the objective verification analysis. The green area in the flowchart in **Figure 7** provides a graphical representation of the steps described in sections 4.2.2 and 4.2.1.

4.1 Definition of the verifying rainfall thresholds (VRTs)

If not known a priori, VRT magnitudes can be defined in several ways (see **Figure 7**, green area “Definition of VRTs”). If point rainfall observations are available (e.g., rain gauges or radars), one can create the distribution of the observed flash-flood-triggering rainfall totals. VRTs would then correspond to the specific percentiles of the distribution. The higher the percentile, the higher the magnitude of the VRT, and the higher the severity level of flash flood events considered in the objective verification analysis. This approach requires high-density rainfall observations, in both space and time, to capture the extreme (localised) rainfall totals that trigger flash floods (Haiden and Duffy 2016; Ramos Filho et al. 2021). In the absence of a suitable observational network (for example, in Ecuador, no high-density, in situ 12-hourly rainfall observations are available), the VRTs can be defined only from gridded rainfall products such as reanalysis such as ERA5 (Hersbach et al. 2020), reforecasts (Hamill et al. 2006), or blended gridded rainfall observations such as MSWEP (Beck et al. 2019) or GPCP (Adler et al. 2018). However, these datasets tend to underestimate rainfall extremes because of their coarse resolution (Tapiador et al. 2019).

This study proposes a methodology for creating a synthetic distribution of flash-flood-triggering rainfall events using short-range ecPoint-Rainfall forecasts (**Figure 7**, pink area). At short-range leads, the ecPoint-Rainfall realisations can be considered proxies for point rainfall observations within the grid boxes (Hewson and Pillosu 2021). Each of the N flood reports is associated with ecPoint-Rainfall forecasts from the nearest grid box (**Figure 8a**). At each forecast run, two 12-hourly accumulation periods span each flood report’s reporting time (see the first and second columns of **Table 4**), so a

distribution of 396 ecPoint-Rainfall realisations (that is, 99 ecPoint-Rainfall values \times 2 accumulation periods \times 2 runs) can be built for each flood report (blue lines in **Figure 8b**). Owing to the high number of forecast realizations per flood report, only one year of short-range forecasts is sufficient to define the VRTs. The rainfall value (tp) associated with the X^{th} percentile of the distribution (red dots in **Figure 8b**) characterizes a certain level of severity for a flash-flood-triggering rainfall event. The net distribution of the $N tp(x^{\text{th}})$ values (red line in **Figure 8c**) represents the distribution of flash-flood-triggering rainfall events. Several percentiles were tested. They were supposed to be reasonably high to exclude low rainfall totals from the analysis that were unlikely to be the drivers of any flash flood event. This study tested the 50th, 75th, 85th, 90th, 95th, 98th, and 99th percentiles. Two flash-flood-triggering rainfall severity categories were considered in this study, moderately severe (MS) and severe (S). To define the range of rainfall totals that were moderately severe (tp_{MS}) and severe (tp_{S}), a rainfall distribution was built from a time series of 10 years SYNOP observations. For this study, tp_{MS} lies in the rainfall values between the 95th and 99th percentiles, while tp_{S} lies between the 99th and 99.99th percentiles (**Figure 8d**). These two ranges can then be used to determine which X^{th} percentiles should be considered to define moderately severe flash-flood-triggering rainfall events and severe flash-flood-triggering rainfall events. The corresponding VRT_{MS} and VRT_S were then defined by deciding how many flood reports would like to be retained in the analysis, for example, the top 1/4, 1/2, or 3/4 (**Figure 8e**). The decision depends on the number of reports available at the beginning of the analysis to maintain a reasonable number of events that will produce a robust statistical analysis. In this study, we maintained the top 3/4 flood events. Separate VRTs were calculated for "La Costa" and "La Sierra" to capture their hydro-climatological regimes.

294 4.2 Objective verification to assess the rainfall forecasts' performance in the identification 295 of areas at flash flood risk

296 4.2.1 Assessment of forecasts' discrimination ability: Receiver Operating Characteristic 297 (ROC) curves and Area Under the ROC curve (AROC)

298 This study used the Relative Operating Characteristic (ROC) curve and the area under the ROC curve (AROC) to estimate
299 and compare the discrimination ability of ENS and ecPoint rainfall forecasts in the prediction of areas at risk of flash
300 floods(Jolliffe and Stephenson 2011). ROC curves were constructed using a 2×2 contingency table that quantifies the hits
301 (H), misses (M), false alarms (FA), and correct negatives (CN) that occur when action is advised based on the VRT exceeding
302 each sampled probability threshold (see **Table 3** for the definition of the constituting elements of the contingency table).
303 Correspondent hit rates (HR) and false alarm rates (FAR) can be then computed, respectively, from equations (1) and (2):

$$\text{HR} = H / (H+M) \text{ [values between 0 and 1]} \quad (1)$$

$$\text{FAR} = FA / (FA+CN) \text{ [values between 0 and 1]} \quad (2)$$

304 For each sampled probability threshold, the ROC curves map HRs on the Y-axis against FARs on the X-axis. The location
305 of the ROC curve in the graph and the geometrical area under the ROC curve (AROC) determine the discrimination ability
306 of the forecasting system. Perfect discrimination is obtained when only HRs grow, whereas the FARs always remain equal
307 to zero. This is represented by an ROC curve that rises from the bottom left corner (0,0) along the Y-axis to the top-left
308 corner (0,1) and moves straight to the top-right corner (1,1). In this case, the AROC was equal to 1. When the forecasting
309 system has no discriminatory ability (i.e., it does not provide any additional information beyond climatological predictions),
310 the HRs and FARs grow at the same rate. Therefore, the ROC curve lies along the diagonal of the graph, and the AROC is
311 equal to 0.5.

312 How ROC curves are built and AROCs are computed has a significant impact on the interpretation of the results. To
313 ensure that the ROC curves are as complete as possible, probability thresholds are determined using the full discretization
314 available in the ensemble, rather than using fixed percentage bins(Ben Bouallègue and Richardson 2022). Hence, ROC
315 curves for ENS and ecPoint were constructed with 51 and 99 points, respectively. No curve fitting was used to build or
316 complete the ROC curves, and straight lines were drawn between consecutive points in the graph, as well as the last
317 meaningful point of the ROC curve and the top-right corner(Ben Bouallègue and Richardson 2022). Moreover, AROCs are
318 computed using trapezoidal approximation, which simply sums the areas of single trapeziums formed by the straight lines
319 between the ROC's consecutive points. As a result, ROC curves for high VRTs might cluster on the bottom left corner of the
320 graph, and if built with fewer points, they might look incomplete, and AROCs might result in smaller. However, this approach
321 focuses on the analysis of "real" and not on the "potential" discrimination ability of rainfall forecasts. The percentile
322 bootstrapping technique was applied to evaluate whether the differences between the AROC for ENS and ecPoint were
323 significant(DiCiccio and Efron 1996). Sampling with replacement with 10,000 replicates and 95% confidence intervals were
324 considered.

325 Populating the contingency tables (**Table 3**) is one of the challenges of this objective verification analysis. Stationary
326 observations (i.e., provided by instruments installed at a specific location, e.g., rain gauges) provide time series that record

327 both yes and no events at the location where the instrument was installed. Thus, all four elements in the contingency table
 328 were quantified. Non-stationary observations record only yes events at the location where the events occurred. As a result,
 329 it is impossible to answer the question “*if there are no reports in an area, is it because an event happened, but nobody
 330 reported it, or because there was no event to report?*”. Some studies verify only yes-events with the caveat that only
 331 quadrants I (i.e., hits) and III (i.e., misses) of the contingency table can be populated(Robbins and Titley 2018). Instead, this
 332 study followed the method of Tsonevsky et al. (2018), which allows the contingency table to be fully populated. This method
 333 assumes that a non-report corresponds to a non-event. Because of the care used to create the observational flood
 334 database, this assumption was also considered valid for this study. Observational fields are built by assigning 1 to grid-boxes
 335 containing at least one flood report (i.e., observational yes-event); otherwise, a value of 0 is assigned (i.e., observational
 336 non-event). Forecast fields are built by assigning a value of 1 to those grid-boxes where the considered VRT is exceeded
 337 with a considered probability threshold (i.e., forecast yes-event); otherwise, the grid boxes are assigned a value of 0 (i.e.,
 338 forecast non-event). The 2X2 contingency tables are built by examining overlapping grid boxes in correspondent
 339 observational and forecast fields; when both grid boxes are assigned a value of 1 or 0, they count as H and CN, respectively.
 340 When a grid box in the observational field is assigned a value of 1, and the corresponding grid box in the forecast field is
 341 assigned a value of 0, it counts as M. It counts as a false alarm (FA) if it occurs, and vice versa.

342 **4.2.2 Assessment of forecasts' calibration: Frequency Bias (FB)**

343 The frequency bias was used to evaluate the reliability of ENS and ecPoint rainfall forecasts in the prediction of areas at
 344 risk of flash floods. For each lead time, the frequency bias was determined by dividing the total number of ensemble
 345 members exceeding the considered VRT by the product of the number of ensemble members and total number of instances
 346 when a flash flood was observed. Equation (1) was used to compute the FB:

$$347 \text{FB} = \frac{\sum_{i=1}^M \sum_{j=1}^N n_i \text{ ensemble members exceeding VRT}}{(n_i \text{ ensemble members}) * (\sum_{i=1}^M \sum_{j=1}^N n_i \text{ instances when a flash flood was observed})} \quad (3)$$

347 A bias score of 1 indicates perfect calibration, with scores greater and smaller than 1 indicating that the forecasting
 348 system over- and under-predicts the observed events, respectively. It is worth noting that FB measures the overall ratio of
 349 forecast events to observed events. As such, it can provide a score of 1 when there are compensating errors. It can also be
 350 observed that a forecasting system overestimates the observed events if they are heavily underreported.

351 **5 Results**

352 **5.1 Verifying rainfall thresholds**

353 The rainfall climatology from SYNOP observations in “La Costa” (**Figure 9a**) shows that the ranges for tp_{MS} (between 10
 354 and 45 mm/12h) and tp_s (between 45 and 108 mm/12h) are much bigger than in “La Sierra” where tp_{MS} ranges between 5
 355 and 25 mm/12h and tp_s ranges between 25 and 65 mm/12h (**Figure 9c**). It was decided to define the VRT by maintaining
 356 the top 3/4 of the flood reports with $EFFCI \geq 6$ to generate robust statistics. Considering this, the net distributions of rainfall
 357 events associated with flash floods corresponding to the 50th and 75th percentiles provide rainfall values that are deemed
 358 too small in both regions (**Figure 9b** and **Figure 9d**). The net distributions for the 85th, 90th, 95th, and 98th percentiles provide
 359 candidates for defining the VRT_{MS} in both regions. To increase the number of rainfall events, the VRT_{MS} was defined using
 360 the net distribution for the smallest percentile (i.e., the 85th). Only the net distribution for the 99th percentile is a candidate
 361 for defining the VRT_s . The VRT_{MS} and VRT_s are indicated by purple and orange dots in **Figure 9c** for “La Costa” and **Figure 9f**
 362 for “La Sierra.” The rounded values in mm/12h, used in the objective verification analysis are listed in **Table 4**. It is worth
 363 noting that VRT_{MS} is similar in both regions (10 mm/12h in “La Costa” and 6 mm/12h in “La Sierra”), while VRT_s in “La Costa”
 364 (50 mm/12h) is twice as much as in “La Sierra” (26 mm/12h).

365 **5.1.1 Forecast's discrimination ability**

366 **Figure 10** shows the evolution of the AROC with the lead time for VRT_{MS} and VRT_s for “La Costa” and “La Sierra.” No
 367 degradation with lead time in the AROCs was observed in “La Costa” (**Figure 10a** and **Figure 10b**), while there is some
 368 degradation observed in “La Sierra” (**Figure 10c** and **Figure 10d**). The AROCs for ENS and ecPoint diminished at the same
 369 rate for both VRT. Overall, the AROC values were larger for VRT_{MS} (**Figure 10a** and **Figure 10c**) than for VRT_s (**Figure 10b** and
 370 **Figure 10d**), and for “La Costa” (**Figure 10a** and **Figure 10b**) compared to “La Sierra” (**Figure 10c** and **Figure 10d**). A feature
 371 that stands out in all panels in **Figure 10**, but especially in “La Costa,” is the sinusoidal pattern shown by the AROC in
 372 correspondence of the different accumulation periods throughout the day. In “La Costa” (**Figure 10a** and **Figure 10c**), the
 373 peaks in the AROC are observed between 0000-1200 LT (i.e., lead time steps labelled in purple) and 0600-1800 LT (i.e., lead
 374 time steps labelled in cyan, that correspond to rainfall occurred mainly during daytime), while troughs are mostly observed
 375 between 1200-0000 LT (i.e., lead time steps labelled in pink) and 1800-0600 LT (i.e., lead time steps labelled in green, that

correspond to rainfall occurred mainly during nighttime). Overall, the discrimination ability for ecPoint in "La Costa" tended to be better than the discrimination ability for ENS, especially for VRT_S (**Figure 10c**). However, it is worth noting that ecPoint and ENS's AROCs are closer in the peaks and further apart in the troughs, meaning that the improvements that ecPoint brings in the identification of areas at risk of flash floods are mainly over rainfall events occurring in the daytime. A similar sinusoidal pattern, although noisier, was observed for the AROCs in "La Sierra" (**Figure 10c and d**). Unlike in "La Costa", in "La Sierra" there are no specific times of the day where ecPoint adds value to the performance of ENS. For VRT_{MS} (**Figure 10c**), ENS shows an overall better discrimination ability than ecPoint, while the latter shows an overall better performance than ENS in the AROCs for VRT_S (**Figure 10d**).

The analysis of the ROC curves provides further information on the discrimination ability of forecasts. **Figure 11** shows the ROC curves for ENS (in red) and ecPoint (in blue) for the 12-hourly accumulation period ending at t+72 (i.e., day 3 forecast), which corresponds to a mainly daytime rainfall whose valid accumulation period ends at 1800 LT. For both regions, the AROC is larger. However, substantial differences were observed in the shapes of ROC curves. For "La Costa" (continuous line), the ROC curves are mostly overlapping, and only the points corresponding to the two top percentiles in ecPoint (98th and 99th) are above the ROC curve for ENS. This means that the underlying curve for ENS and ecPoint is the same, and the greater AROC from ecPoint is due to the capability to identify extremes better thanks to the bigger number of ensemble members. In this case, it can be concluded that the ENS contains the information required to predict whether an extreme flash-flood-triggering rainfall event might occur, although it might not be possible to predict the actual magnitude of the event. To achieve this goal, forecasts from ecPoint are better suited because they can double the hit rate from the ENS with only a very small increase in the false alarm rate. On the contrary, although noisy, it can be observed that the ROC curves in "La Sierra" (dashed lines) do not overlap. This implies that the underlying curves for ENS and ecPoint are different. Thus, ecPoint can identify events for which ENS may not provide any signal.

5.1.2 Forecast's frequency bias

Figure 12 shows the evolution of the FB with lead time for VRT_{MS} and VRT_S, for "La Costa" and "La Sierra." No significant degradation in FB was observed with the lead time in either region. Overall, FB is larger for VRT_{MS} (**Figure 12a** and **Figure 12c**) than for VRT_S (**Figure 12b** and **Figure 12d**), and for "La Sierra" (**Figure 12c** and **Figure 12d**) than for "La Costa" (**Figure 12a** and **Figure 12b**). In "La Costa," ecPoint diminishes the FB at all lead times, but especially for the accumulation period that ends at 0000 LT (steps indicated in pink) in the case of VRT_{MS} and for the accumulation period that corresponds to mainly nighttime rainfall and ends at 0600 LT (steps indicated in green) in the case of VRT_S. For the latter, only accumulation periods that correspond mainly to daytime rainfall and end at 1800 LT (steps indicated in cyan) show a slightly worse FB for ecPoint compared to ENS. ecPoint's FB for VRT_{MS} in "La Sierra" (**Figure 12c**) is significantly better than ENS'FB, while for VRT_S (**Figure 12d**) it is worse, with the exception of the accumulation periods that correspond mainly to nighttime rainfall and end at 0600 LT (steps indicated in green). It is worth noting that opposite to what happens in "La Costa" where the performance is qualitatively the same for both forecasting systems (i.e., the peaks and troughs are observed for the same accumulation periods in both ENS and ecPoint), in "La Sierra" peaks and troughs happen in different accumulation periods for different forecasting systems. For VRT_{MS}, peaks occurred for daytime rainfall in the ENS and for nighttime rainfall in ecPoint. The opposite is true for the VRT_S.

A feature that stands out in all panels in **Figure 12** is that the FB values are significantly larger than 1 (i.e., the perfect value for FB), indicating that ENS and ecPoint significantly overestimate the frequency of flash flood events. **Figure 13** shows the counts of yes-events in forecasts and observations for a day 3 forecast (i.e., accumulation period ending at t+72). In "La Costa" (**Figure 13a** and **Figure 13b**) there is a good overall correspondence between days with yes- and non-flash-flood events, especially for VRT_S. The larger FB is mainly due to the slightly larger count of grid-boxes corresponding to yes events in the forecasts. In "La Sierra" (**Figure 13c** and **Figure 13d**), there is also a good representation of the periods with yes- and non-flash-flood events, especially for VRT_S. However, the count of grid-boxes corresponding to yes-events in the forecasts is much larger than in the observations, contributing to FB values that are well above the perfect value of 1.

6 Case Study: intense rainfall and flash floods on 8th March 2021

This analysis is presented to further support the outcomes of the objective verification analysis. March is one of the wettest months in 2021 in Ecuador. As a result of numerous heavy rainfall events, rivers such as Guayas, Los Ríos, Esmeraldas, and Manabí burst their banks, with landslides being observed in many different regions. The 8th of March was one of the wettest days (**Figure 14a**). Significant impacts⁴ were mainly observed in the highly populated city of Guayaquil, where very heavy rainfall was reported to occur in the afternoon after 4 pm (Local Time, LT), with rainfall totals exceeding 100 mm/24h⁵ in the city centre (zoomed red area in **Figure 14a**). Around 8th March, the MJO was reported by various centres to be in phase 8⁶, which tends to be conducive to, or at least correlated with, onshore lower tropospheric westerly

⁴ <https://www.eluniverso.com/guayaquil/comunidad/la-mayor-lluvia-del-2021-en-guayaquil-provoco-afectaciones-en-64-zonas-entre-inundaciones-arboles-caidos-canales-rebosados-y-otros-nota/>

⁵ <https://www.wunderground.com/history/daily/SEGU/date/2021-3-8>

⁶ https://www.cpc.ncep.noaa.gov/products/precip/CWlink/MJO/ARCHIVE/PDF/mjo_evol-status-fcsts-20210315.pdf

wind anomalies near the equatorial west-facing coasts of South America (Wheeler and Hendon 2004). In conjunction, analysts from the NOAA have highlighted the likelihood of enhanced convective activity in the region of routine bulletins. From the dawn of 8th March, ECMWF's numerical model sounding (**Figure 14b**) appeared particularly conducive to flash-flood-triggering rainfall activity. For instance, the very high Convective Available Potential Energy (CAPE) shows that there is potential for sufficiently high dew point depression insolation-based triggering that might not be impeded by thick clouds. It also shows the potential for very high-altitude convective cloud tops, very strong wind shear that favours prolonged convective cell life cycles (as down-draughts would not interfere with up-draughts), and relatively light steering winds (favouring slow movement of convective cells). This description is supported by SYNOP and METAR observations and satellite imagery (not shown), suggesting that the cause of this rainfall event was organized convective cells, whose development was triggered by insolation.

Figure 14c shows the ENS and ecPoint forecasts from the 00 UTC run for day 1 (first row), day 3 (second row), and day 7 (third row) lead times. The forecasts are valid for the 12-hourly accumulation period between 8th March 8, 2021, at 12 am and 9th March 9, 2021, at 0 am (LT), that is, the fraction within the 24-hourly period of the observations reported in **Figure 14a** when most of the rainfall fell. Forecasts for the 50th (first and second columns), 95th (third and fourth columns), and 99th percentiles (fifth and sixth columns) are shown. The median (i.e., 50th percentile) represents the dividing line for the equi-probable observation categories. By comparing the rainfall observations (**Figure 14a**) and the forecast for the 50th percentile (first and second columns in **Figure 14c**), it can be seen that, overall, the ENS overestimates the mean rainfall. On the contrary, owing primarily to its bias correction for rainfall overprediction at the grid-scale, ecPoint's 50th percentile is systematically smaller than in the ENS, showing a better fit with the observations. At the same time, ecPoint's 95th (third and fourth columns in **Figure 14c**) and 99th percentiles (fifth and sixth columns in **Figure 14c**) highlight a higher potential than the ENS for having higher local rainfall totals in certain areas (e.g., Guayaquil). While far more observations would be needed to analyse the performance of ENS and ecPoint forecasts for such high percentile robustly, it appears that both ENS and ecPoint predicted well the local rainfall extremes in "La Costa." For example, there is a signal of extreme rainfall in the ENS for Guayaquil at the 95th percentile). In contrast, it appears that ecPoint adds the most value to the prediction of extreme rainfall in "La Sierra." For example, ecPoint's 99th percentile shows a 1% chance of having up to 60 mm/12h at some location in "La Sierra", and one location observed such amount.

454 7 Discussions

455 7.1 Can short-range ecPoint rainfall forecasts be used as proxy for in-situ observations in 456 data scarce regions to calculate VRT?

457 The literature shows that the definition of flash-flood-triggering rainfall thresholds consists in a still widely used way to
458 predict areas at risk of flash floods. Filho et al. (2021) proposed an improved rainfall-threshold approach for robust
459 prediction of flood and flash flood hazards in São Paulo, Brazil. Ma et al. (2021) developed a new rainfall-triggering index
460 for flash flood warning in Yunnan, China, underlining the rapid, short-duration, and high-velocity flows characteristic of
461 flash floods. Papagiannaki et al. (2015) identified specific flash-flood-triggering rainfall thresholds in Attica, Greece, linking
462 them to flash flood impacts. Central to these studies is the need for high-density rainfall observations to establish thresholds
463 without excessive over- or underprediction biases. The lack of high-density, in situ 12-hourly rainfall observations in Ecuador
464 would have limited the ability of defining the flash-flood-triggering rainfall thresholds, used in this study as VRTs. The
465 method for calculating VRTs using ecPoint rainfall forecasts as a proxy for in-situ observations addresses this data gap by
466 simulating a very high-density observational system in the proximity of the flash flood report. However, the probabilistic
467 nature of the ecPoint output puts the following question: of all ecPoint's rainfall realizations associated to a flash flood
468 report, which amount represents better the one that triggered the corresponding flash flood event? The comparison of net
469 distributions of potential flash-flood-triggering rainfall events with observational rainfall climatologies is essential to
470 distinguish between net distributions that represent "moderately severe" rainfall events, that might or might not generate
471 flash floods, from net distributions that represent "severe" rainfall events, that are very likely to generate flash floods most
472 of the times.

473 Several studies have found that flash flood forecasts are very sensitive to rainfall's spatial-temporal variability (Douinot
474 et al. 2016; Song et al. 2019; Norbiato et al. 2008; Borga et al. 2014; Demissie et al. 2021). While the average rainfall does
475 not seem to vary significantly in "La Sierra," the coastal areas in "La Costa" appear drier than on the western slopes of the
476 Andes, suggesting that more than one VRT may be required. Furthermore, the differences between daytime and nighttime
477 rainfall amounts suggest that a distinction between VRTs for daytime and nighttime events could be beneficial to reduce
478 biases in the verification analysis. Due to the limited availability of observational data, it was decided to aggregate all these
479 conditions to provide more robust results, and only two VRTs were computed, one for the entire "La Costa" and one for
480 the entire "La Sierra". However, this data aggregation comes at the expense of a greater granularity that might be beneficial
481 and required to predict better areas at risk of flash floods better. Finally, focusing solely on rainfall when defining VRTs may
482 overlook other important factors. Dinis et al. (2021) highlighted how terrain and urban planning influence flash flood
483 vulnerability in Benguela, Angola, even under moderate rainfall. Therefore, a more comprehensive approach incorporating

484 geomorphological, socio-economic, and environmental factors alongside rainfall data is imperative for refining further the
485 flash flood predictions and reducing false alarms.

486 7.2 How do ENS and ecPoint's performance compare in the prediction of areas at risk of 487 flash floods?

488 In Section 2, we learned that the meteorological dynamics influencing rainfall in "La Costa" and "La Sierra" are
489 distinctively different. This contextual backdrop is essential for interpreting the ENS and ecPoint performance in the
490 identification of areas at flash flood risk in the two regions. In "La Costa", flash-flood-triggering rainfall events are generated
491 predominantly by large-scale convective systems such as El Niño and the MJO (Tobar and Wyseure 2018; Recalde-Coronel
492 et al. 2020). ENS can predict with a reasonable degree of accuracy up to six weeks ahead these systems (Haiden et al. 2021).
493 Ergo, ENS can proficiently identify areas at risk of heavy rain (and flash floods), albeit it might still mis-forecasts the absolute
494 rainfall amounts. Herein, ecPoint's contribution is primarily confined to rectifying the rainfall estimates. This type of
495 correction is influential in continuous rainfall amount verification, but it becomes less relevant in binary event verification.
496 Namely, it is not significant if a yes-event is obtained from exceeding the VRT by 1 mm or 20 mm as far as it is exceeded,
497 and the correction of the absolute rainfall totals will matter only when it tips the balance between having or not having a
498 yes-event. This behaviour can be observed for corrections applied by ecPoint to daytime and nighttime rain in "La Costa".
499 The needed reduction of daytime rain in "La Costa" applied by ecPoint to ENS forecasts is rewarded by both AROC and FB
500 metrics. However, no significant changes in performance are observed when unnecessary corrections are applied to
501 nighttime rainfall (because the post-processing does not differentiate bias corrections depending on LT): ecPoint's AROC
502 values are the same as those for ENS, and the FB values are only slightly inferior. Conversely, flash-flood-triggering rainfall
503 events in "La Sierra" are generated predominantly by small-scale convective systems (Recalde-Coronel et al. 2014). ENS
504 struggles to capture extreme rainfall from such systems even on day 1, and when it does, its predictive skill decreases
505 significantly after a few days (Haiden et al. 2023). Hewson and Pillosu (2021) have shown that ecPoint significantly enhances
506 the detection of small-scale convective systems and increases the lead time at which these systems can be identified in
507 forecasts. As such, ecPoint has shown to perform better in identifying areas at risk of flash floods, especially for the most
508 extreme flash flood events. The case-study-based analysis in Section 6 aligns with the discussion above.

509 These findings underscore the importance of considering the scale and nature of the weather systems that generate
510 extreme rainfall in the region of interest when evaluating rainfall forecast performance in the identification of areas at risk
511 of flash floods. When considering small-scale convective systems, ecPoint enhances structurally the performance of ENS,
512 while whenever the main cause of extreme rainfall is a large-scale system, ENS can do a respectable job, and ecPoint would
513 mainly help in predicting more accurately the entity (in mm) of the flash-flood-triggering rainfall events. This is consistent
514 with the findings in Bucherie et al. (2022), who showed that larger-scale patterns linked to the occurrence of flash floods
515 can be discerned in coarser global-scale models. This result is paradigm-changing. So far, the research and the forecasting
516 community have believed that km-scale rainfall forecasts were needed to identify areas at flash flood risk. However, this
517 study establishes that raw global rainfall forecasts can be successfully used in the identification of areas at risk of flash
518 floods under certain weather conditions. The two main benefits of being able to use global raw and post-processed NWP
519 rainfall forecasts are (1) the availability of rainfall forecasts over a continuous domain (no more patchy coverage of km-
520 scale limited-area models or radar-derived products) and (2) the availability of predictions up to medium-range lead times
521 (instead of just a few hours or a couple of days).

522 7.3 How adequate is impact data to verify flash floods?

523 This study demonstrates that enhanced flood report databases, such as the one developed in Ecuador by Kruczakiewicz
524 et al. (2021b), are instrumental in setting flash-flood-triggering rainfall thresholds and assessing rainfall forecast
525 performance in flash flood prediction. The better and more reliable spatial/temporal coverage of the flood reports in
526 Ecuador's database enabled an in-depth, long-term assessment that would have been unfeasible with publicly available
527 flood reports due to their inevitably poorer spatial/temporal coverage and poorer identification of flood features (e.g., type
528 of flood). For these reasons, flash flood verification in the past was primarily based on case studies as more detailed
529 information was available for single events (Gaume et al. 2009). While a case-study-based verification approach is
530 invaluable to understanding how forecasts predict flash flood events, provided enough observations are available, the
531 results might not hold to other events due to the focused nature of the analysis. Alternatively, taking advantage of the
532 better quality and spatial coverage of rainfall observations, researchers might use them to infer the performance of rainfall
533 forecasts in predicting flash floods. However, as seen in this study, the results of these two verification analyses are
534 different. ecPoint almost always performs better than ENS in predicting extreme (localized) rainfall (Hewson and Pillosu
535 2021; Gascón et al. 2023; Hemri et al. 2022). However, in predicting the areas at risk of flash floods, the verification results
536 are more nuanced, and we would do a disservice to the ENS forecasts by not considering these two research questions
537 separately. Thus, this study underscores the importance of enhancing flash flood report databases to assess better the
538 performance of rainfall forecasts for flash flood prediction, contributing significantly to more effective disaster
539 preparedness and risk management strategies.

540 Although this dataset is the best attempt to build a comprehensive historical record of flash flood events in Ecuador,
541 event underreporting still needs to be addressed to provide a more comprehensive assessment of forecast performance.
542 In alignment with previous studies attempting to use impact-based observations to estimate forecast performance (Mitheu
543 et al. 2023; Robbins and Titley 2018; Hitchens et al. 2013), the verification of the rainfall forecasts against underreported
544 flash flood events can lead to an underestimation of forecast skill and undermine the confidence in the forecasts, causing
545 the dismissal of valuable predictions crucial for preparedness actions. Therefore, this issue requires who reads the
546 verification results to go beyond the actual numbers and interpret their meaning in a critical, although subjective, way. For
547 example, although the FB is far larger than 1 (that would mean the forecasts massively overestimate the areas at risk of
548 flash floods), the counts of yes-events in the forecast and the observations show there is a good correspondence between
549 wet/dry conditions (meaning the forecasts can identify fairly well which areas are at risk of flash floods) and that the high
550 FB might be due mainly to the low spatial coverage of the reports. Therefore, improvements in the observational spatial
551 coverage could reduce the number of “false” false alarms, which for this type of analysis (using non-standard observations)
552 is the biggest and most difficult problem to address (Marsigli et al. 2021).

553 **8 Conclusions**

554 This study defined a new method to calculate VRTs in data-scarce regions. By using short-range ecPoint rainfall forecasts
555 as proxies for in-situ observations to calculate VRTs, this method addresses significant data gaps that limit the verification
556 and creation of flash flood forecasting systems in data-scarce regions.

557 This study also critically examined the performance of two global rainfall forecasts, ENS and ecPoint, in identifying areas
558 at risk of flash floods in Ecuador. It highlighted the nuances in the performance of the two forecasting systems in different
559 meteorological contexts. While ecPoint outperforms ENS when flash-flood-triggering rainfall events are mainly originated
560 from small-scale convective systems, in the case of large-scale systems ENS and ecPoint show comparable performance in
561 the identification of areas at risk of flash floods, with ecPoint enhancing primarily only the accuracy of the magnitude
562 prediction of the flash-flood-triggering rainfall event.

563 Finally, while the quality of the flash flood report database built for Ecuador is much higher than other public databases,
564 this study has also discussed the impacts in objective flash flood forecast verification of a still large event underreporting.
565 While the enhanced quality of the database used in this analysis allowed the authors to conduct an in-depth, long-term
566 verification analysis, there is still work to do better assess forecast performance to support preparedness and action during
567 decision-making processes.

568 The authors of this study suggest that future research should be focused in two main areas. Since the definition of flash-
569 flood-triggering rainfall thresholds is linked to the availability of flash flood reports and those are not available in equally
570 way around the globe, it would not be possible to develop rainfall-base flash flood forecasting systems over a continuous
571 global domain. It would be interesting to develop an ecPoint-compatible gridded rainfall climatology, for example using the
572 newly developed ERA5-ecPoint (Hewson et al. 2023), to create flash-flood-triggering rainfall thresholds over a continuous
573 global domain and support the development of a rainfall-based flash flood forecasting system over the same domain. The
574 authors also suggest that that more resources are spent in the development of more flood databases like the one presented
575 in this study as they incorporate invaluable details on the type of flood that can be used to target verification and forecast
576 development efforts. At the same time, research efforts should be focused in addressing the uncertainties around the
577 spatial coverage of this type of observations to provide clearer guidance on forecast performance.

Tables

Table 1 - The first column shows the total number of flood reports in the database for 2019 and 2020. The second column shows the number of excluded reports from the study because they did not contain any reporting location (in lat/lon coordinates) and/or reporting time (with date and time). The remaining columns show the distribution of flood reports per region and EFFCI threshold.

Year	N. of raw flood reports	N. of eliminated flood reports	N. of cleaned flood reports	N. of flood reports with $\text{EFFCI} \geq 1$			N. of flood reports with $\text{EFFCI} \geq 6$			N. of flood reports with $\text{EFFCI} \geq 10$		
				Costa	Sierra	Oriente	Costa	Sierra	Oriente	Costa	Sierra	Oriente
2019	302	3	299	176	116	7	93	102	0	17	34	0
2020	190	0	190	96	93	88	48	79	0	22	26	0

Table 2 - Day 1 ecPoint-Rainfall forecasts used to define the verifying rainfall thresholds (VRTs).

Flood reports' reporting time (in UTC for day X)	Valid 12-hourly periods (in UTC) containing the flood reports' reporting time	Correspondent 12-hourly accumulation periods for day 1 ecPoint-Rainfall forecasts (forecast run date / forecast run time in UTC / lead time in hours)
Between 0 and 5.:59	18 (on day X-1) to 5:59	Day(X-1) / 00 UTC / (t+18, t+30) Day(X-1) / 12 UTC / (t+6, t+18) Day(X) / 00 UTC / (t+0, t+12) Day(X-1) / 12 UTC / (t+12, t+24)
	0 to 11:59	Day(X) / 00 UTC / (t+0, t+12) Day(X-1) / 12 UTC / (t+12, t+24) Day(X) / 00 UTC / (t+6, t+18) Day(X-1) / 12 UTC / (t+18, t+30)
Between 6 and 11:59	0 to 11:59	Day(X) / 00 UTC / (t+0, t+12) Day(X-1) / 12 UTC / (t+12, t+24) Day(X) / 00 UTC / (t+6, t+18) Day(X-1) / 12 UTC / (t+18, t+30)
	6 to 17:59	Day(X) / 00 UTC / (t+6, t+18) Day(X-1) / 12 UTC / (t+18, t+30) Day(X) / 00 UTC / (t+12, t+24) Day(X) / 12 UTC / (t+0, t+12)
Between 12 and 17:59	6 to 17:59	Day(X) / 00 UTC / (t+12, t+24) Day(X) / 12 UTC / (t+0, t+12) Day(X) / 00 UTC / (t+18, t+30) Day(X) / 12 UTC / (t+6, t+18)
	12 to 23:59	Day(X) / 00 UTC / (t+12, t+24) Day(X) / 12 UTC / (t+0, t+12) Day(X) / 00 UTC / (t+18, t+30) Day(X) / 12 UTC / (t+6, t+18)
Between 18 and 23:59	12 to 23:59	Day(X) / 00 UTC / (t+12, t+24) Day(X) / 12 UTC / (t+0, t+12) Day(X) / 00 UTC / (t+18, t+30) Day(X) / 12 UTC / (t+6, t+18)
	18 to 5:59 (on day X+1)	Day(X) / 00 UTC / (t+12, t+24) Day(X) / 12 UTC / (t+0, t+12) Day(X) / 00 UTC / (t+18, t+30) Day(X) / 12 UTC / (t+6, t+18)

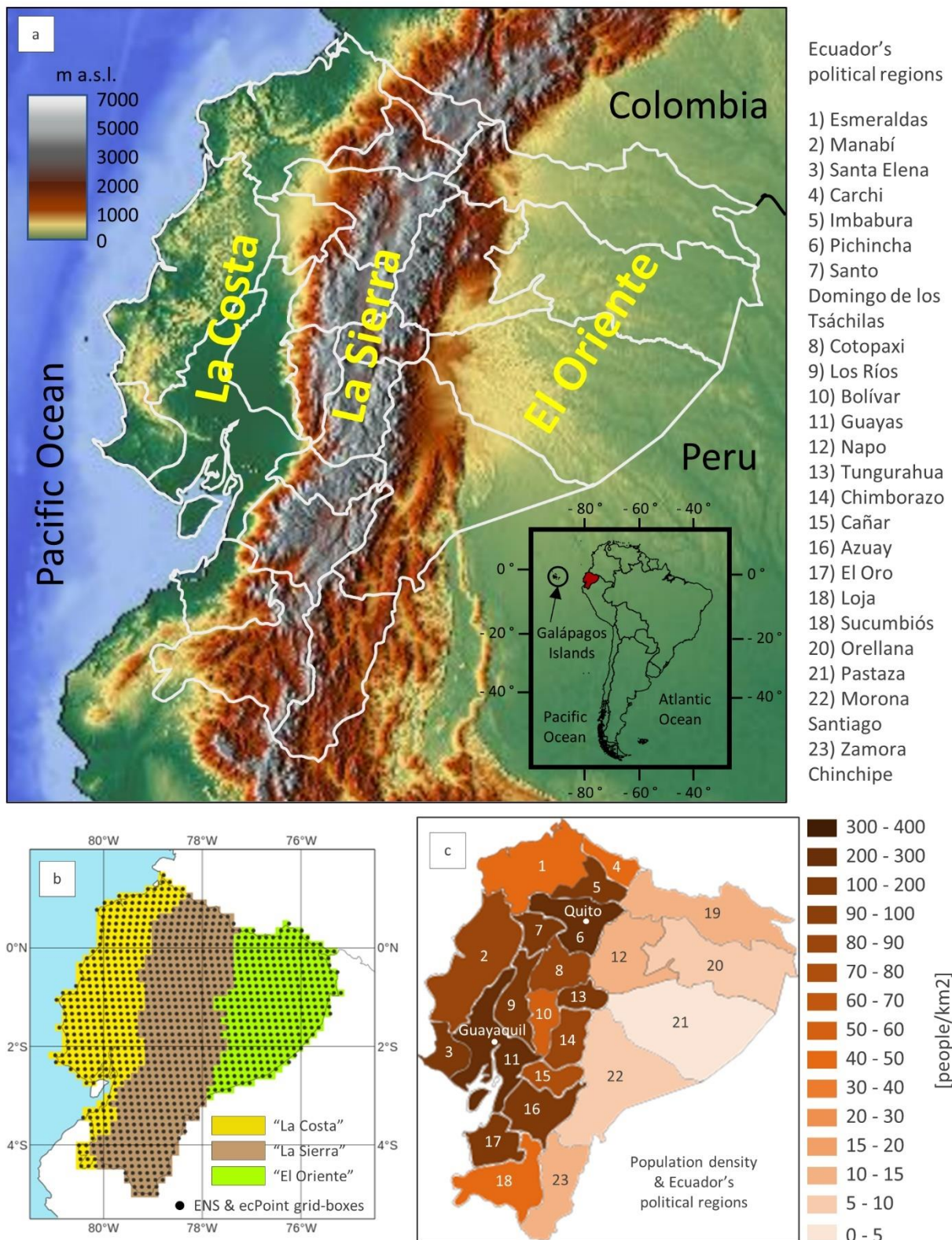
Table 3 - Definition of the four quadrants in a contingency table.

FORECASTS (COLUMNS) / OBSERVATIONS (ROWS)		YES	NO
YES	QUADRANT I Hits (H) <i>The event was observed when it was predicted.</i>	QUADRANT II False Alarms (FA) <i>The event was not observed when it was predicted.</i>	
	QUADRANT III Misses (M) <i>The event was observed when it was not predicted.</i>	QUADRANT IV Correct Negatives (CN) <i>The event was not observed when it was not predicted.</i>	
NO			

Table 4 - Verifying rainfall thresholds (in mm/12h).

Region	VRT85	VRT99
La Costa	9.865 mm/12h (rounded to 10 mm/12h)	50.452 mm/12h (rounded to 50 mm/12h)
La Sierra	5.885 mm/12h (rounded to 6 mm/12h)	25.551 mm/12h (rounded to 26 mm/12h)

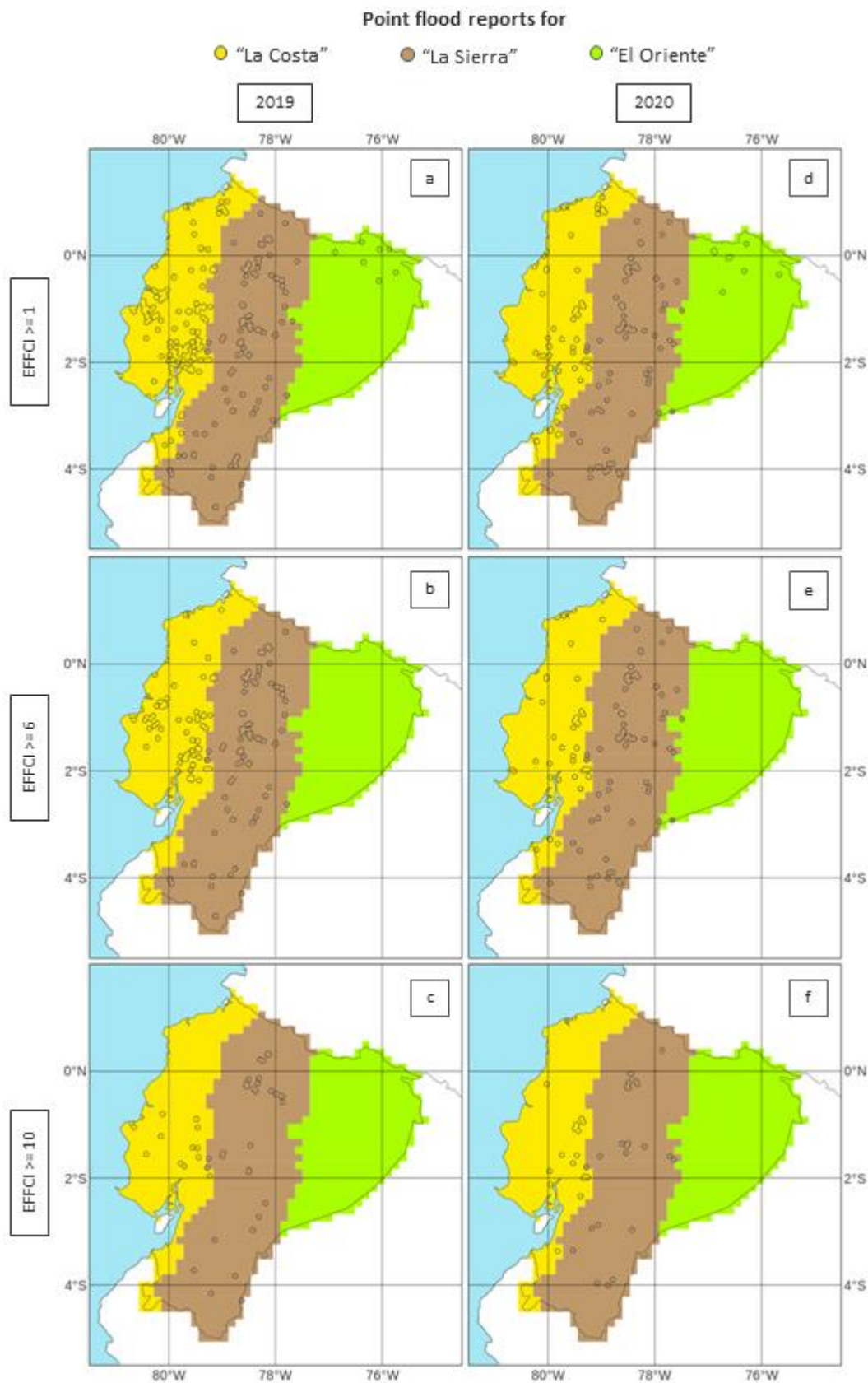
1 Figures



2 **Figure 1** - Panel (a) displays Ecuador's topography, outlines its political regions in white, and indicates the location of the country's three main
 3 geographical regions: the coast ("La Costa"), the Andean highlands ("La Sierra"), and the Amazon forest ("El Oriente"). The insert highlights Ecuador's
 4 location (in red) in South America. Panel (b) shows Ecuador's domain within the ENS and ecPoint grid, with grid boxes indicated with black dots. The
 5 regions are colour-coded in yellow for "La Costa", brown for "La Sierra", and green for "El Oriente". Panel (c) shows the population density from the 2020
 6 census (people/km²) in each political region.
 7

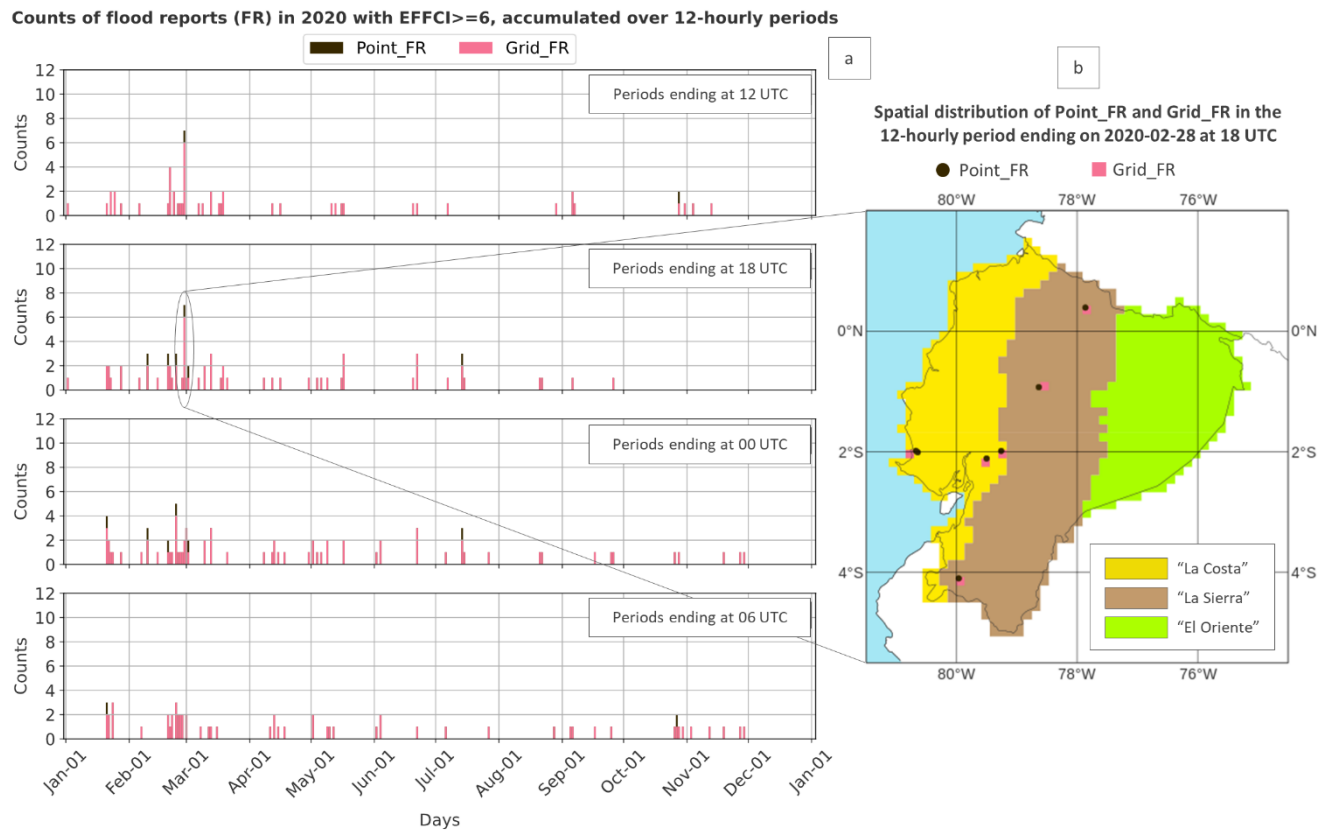
8

9



10 Figure 2 – Panels (a), (b), and (c) show the spatial distribution of point flood reports in 2019 with EFFCIs, respectively, ≥ 1 , 6, and 10. Panels (d), (e),
11 and (f) are the same but for flood reports in 2020.
12

13



14

Figure 3 – Panel (a) displays the timeseries of the counts of 2020's flood reports with $\text{EFFCI} \geq 6$, accumulated over four overlapping 12-hourly accumulation periods, ending at 12 (first row), 18 (second row), 00 (third row), and 06 UTC (fourth row). Figure 2e shows their spatial distribution. Black and pink (overlapped) bars represent point and grid flood reports, respectively. Where the black bars are visible, more than one point flood report was assigned to a grid box. Panel (b) shows the spatial distribution of the point and grid flood reports for the accumulation period that contains the largest number of flood reports, namely the one ending at 18 UTC on 2020-02-28.

15

16

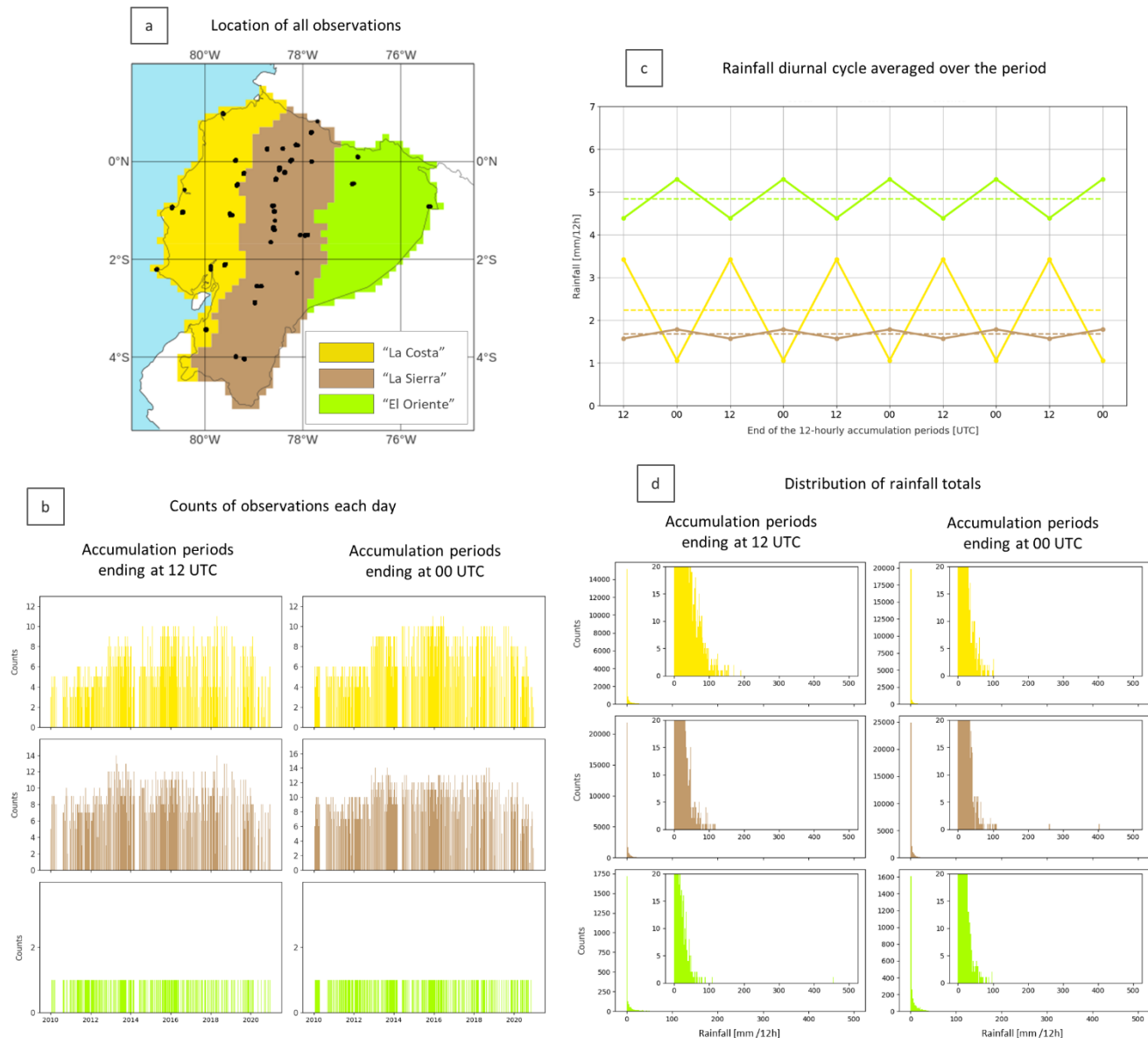
17

18

19

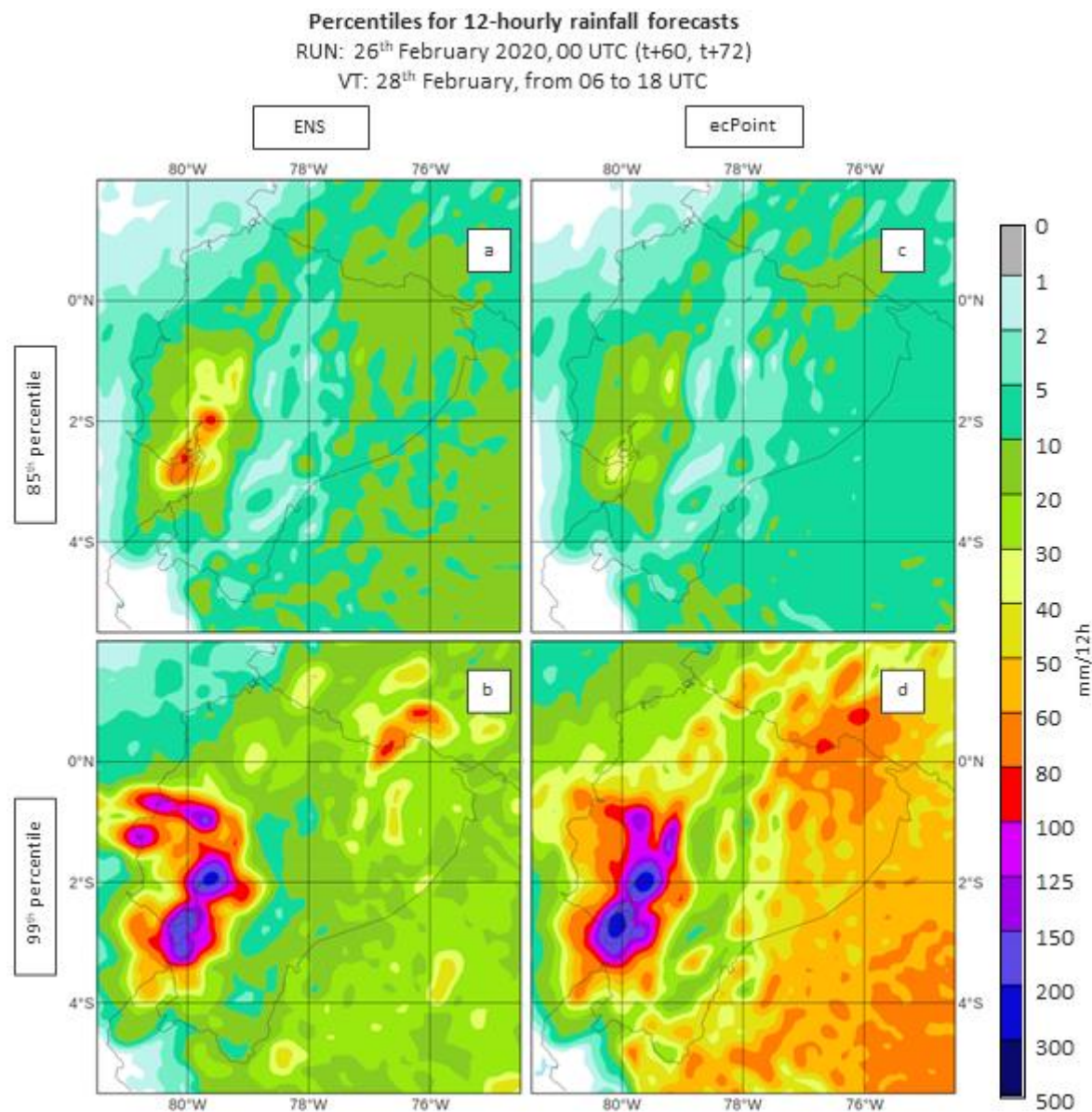
20

Description of SYNOP observations of 12-hourly rainfall between 2010-01-01 and 2020-12-31



21
22 **Figure 4** – Description of 12-hourly SYNOP rainfall observations in Ecuador from 2010-01-01 to 2020-12-31. Only accumulation periods ending at 12
23 and 00 UTC were available. Each plot is colour-coded according to the region they refer to: yellow for “La Costa”, brown for “La Sierra”, and green for “El
24 Oriente”. Panel (a) displays a map plot with the location of all SYNOP observations (some have moved locations over time). Panel (b) shows the daily
25 counts of observations available for the accumulation period ending at 12 UTC (first column) and at 00 UTC (second column). Panel (c) shows the average
26 rainfall for all considered years, for the accumulation period ending at 12 and at 00 UTC (the two values are repeated five times in the plot), and the
27 corresponding trend lines. In panel (d), the distributions of 12-hourly rainfall totals are shown for the accumulation period ending at 12 UTC (first column)
28 and at 00 UTC (second column). Each distribution includes zoomed-in inserts.

29
30
31
32
33



34

35
36
37
38

Figure 5 – Example of a probabilistic ENS (first column) and ecPoint (second column) medium-range rainfall forecast (in mm/12h). The forecast is from the midnight run (00 UTC) on the 26th of February 2020, for the accumulation period ending at t+72, and valid for the 28th of February 2020 between 06 and 18 UTC (i.e., 00 and 12 LT). Panels (a) and (c) show examples of the 85th percentile for ENS and ecPoint, respectively, while panels (b) and (d) show examples of the 99th percentile.

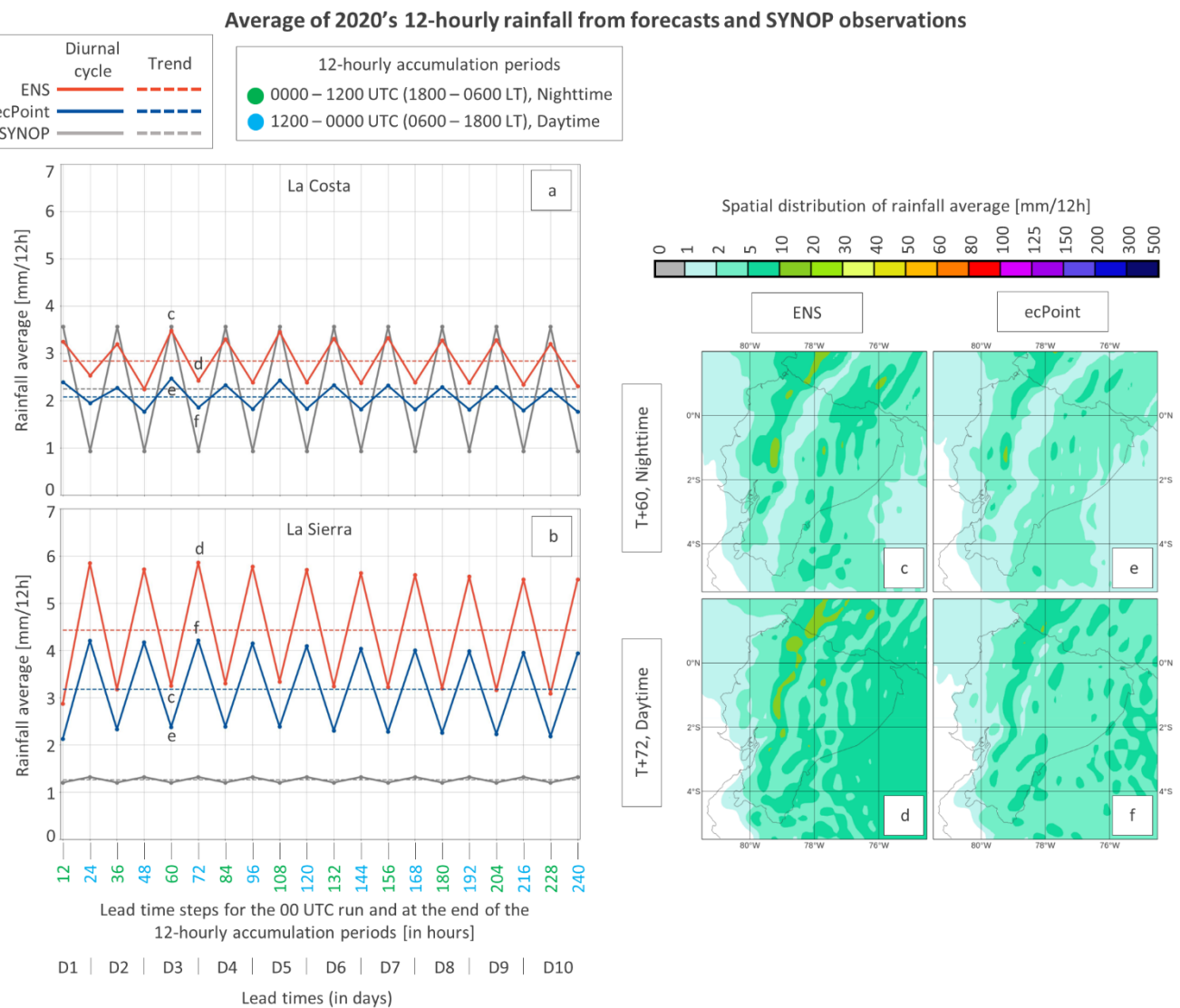


Figure 6 – Panels (a) and (b) show, for “La Costa” and “La Sierra”, respectively, the 12-hourly rainfall average (continuous line) and their trend (dashed line) as a function of forecast lead time up to day 10. SYNOP, ENS, and ecPoint are shown in grey, red, and blue, respectively. The x-axis indicates the lead time steps (in hours) at the end of the 12-hourly accumulation period. Each step is colour-coded according to the valid accumulation period (in UTC and LT) based on the 00 UTC run: the steps representing the accumulation period between 0000-1200 UTC (or 1800-0600 LT, nighttime) are shown in green, while the steps representing the accumulation period between 1200-0000 UTC (or 0600-1800 LT, daytime) are shown in cyan. Panels (c) and (d) illustrate examples of a typical spatial distribution of rainfall averages, respectively, at nighttime and daytime for a day 3 forecast in ENS (accumulation periods ending at steps t+60 and t+72, respectively). Panels (e) and (f) show the same but for ecPoint.

39

40

41

42

43

44

45

46

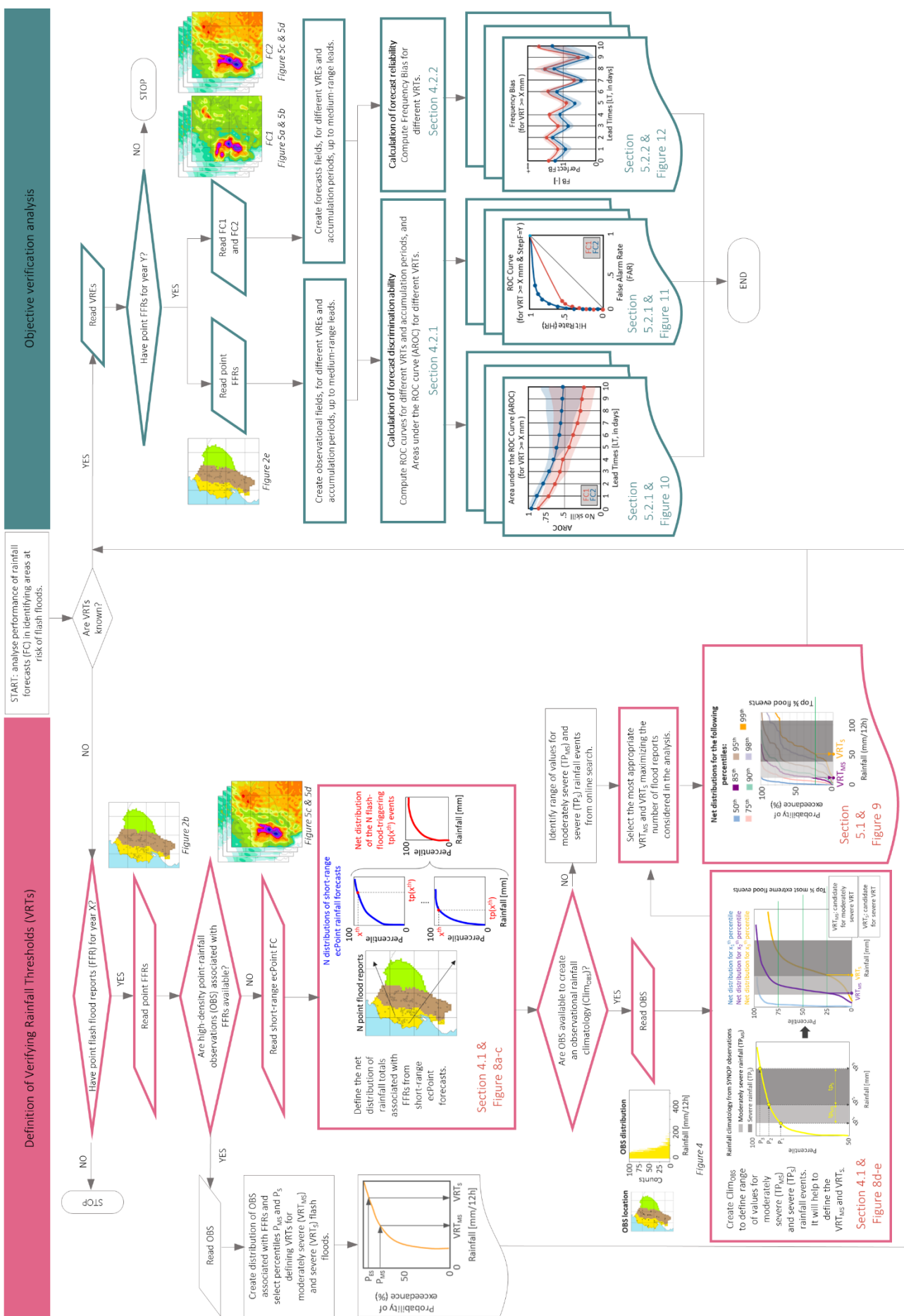
47

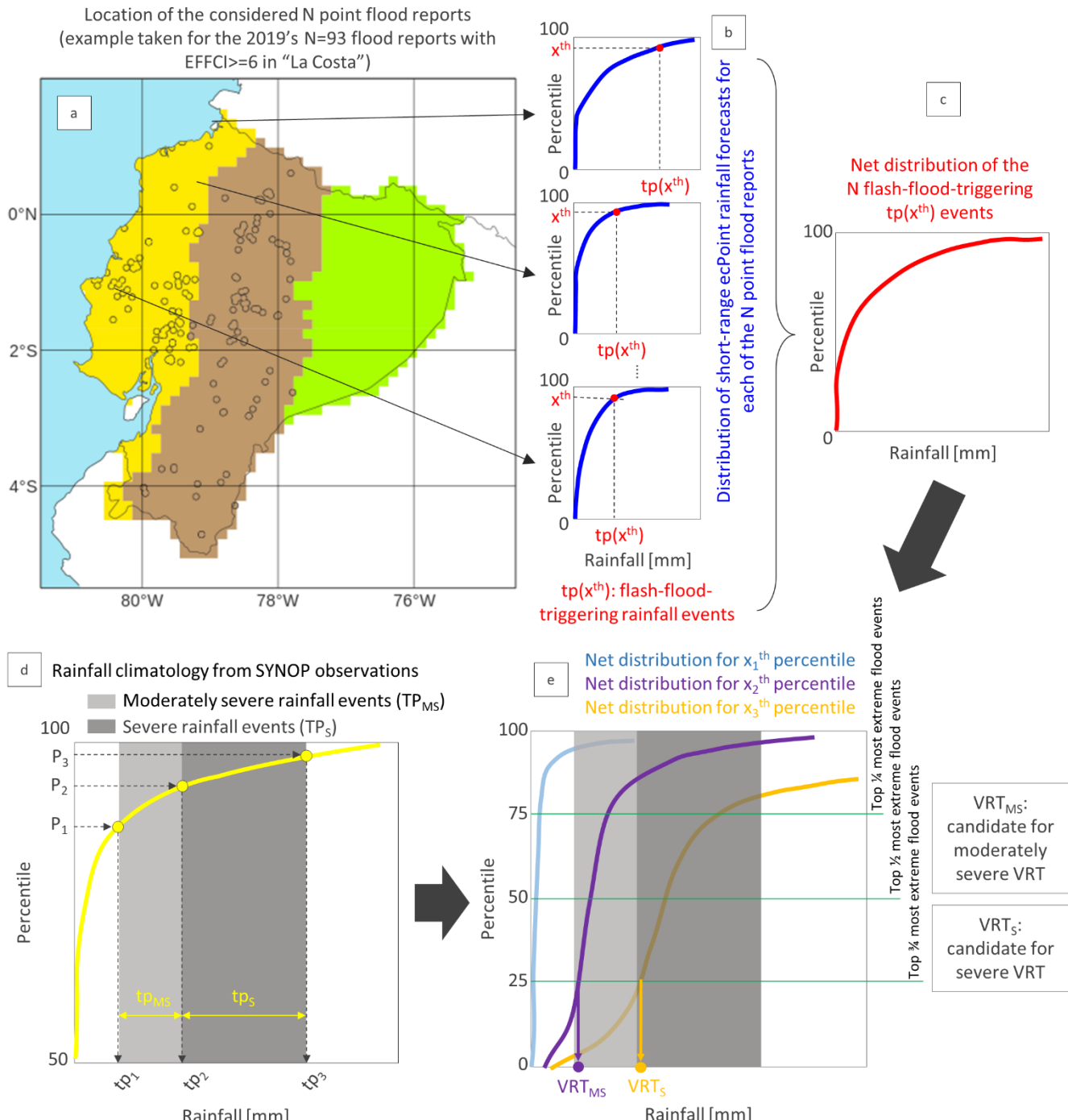
48

49

50

51



Schematic representation of how short-range ecPoint rainfall forecasts are used to determine verifying rainfall thresholds (VRT)


55

56 **Figure 8** – Schematic representation of how short-range ecPoint rainfall forecasts are used to determine verifying rainfall thresholds (VRT) using
57 2019's N=93 point flood reports with $\text{EFFCI} \geq 6$ in "La Costa" as an example (see Figure 2b and Table 1). Panel (a) shows the location of the N point flood
58 reports. Panel (b) shows examples of possible distributions of short-range ecPoint rainfall forecasts associated with each of the N point flood reports (in blue). If a sufficiently large x^{th} percentile is considered in each distribution, the corresponding $\text{tp}(x^{\text{th}})$ values can be regarded as flash-flood-triggering
59 rainfall events (in red). Panel (c) displays the net distribution (in red) of the N flash-flood-triggering rainfall events. In the example, only one distribution is
60 shown. However, as many distributions as desired can be created by considering different percentiles. Panel (d) shows the rainfall climatology (in yellow,
61 as this example refers to "La Costa") built from SYNOP observations. The percentiles P_1 and P_2 , and the corresponding rainfall values tp_1 and tp_2 , define
62 the range of moderately severe rainfall values (tp_{MS}), whose width is visually highlighted by the light grey rectangle. The percentiles P_2 and P_3 , and the
63 corresponding rainfall values tp_2 and tp_3 , define the range of severe rainfall values (tp_S), whose width is visually highlighted by the dark grey rectangle.
64 Using the two rainfall ranges and a pre-established top fraction of the most extreme N flood reports, panel (e) illustrates how candidates for moderately
65 severe VRT_{MS} and severe VRT_S are determined when a series of net distributions of flash-flood-triggering rainfall events are available.

66

67

68

69

70

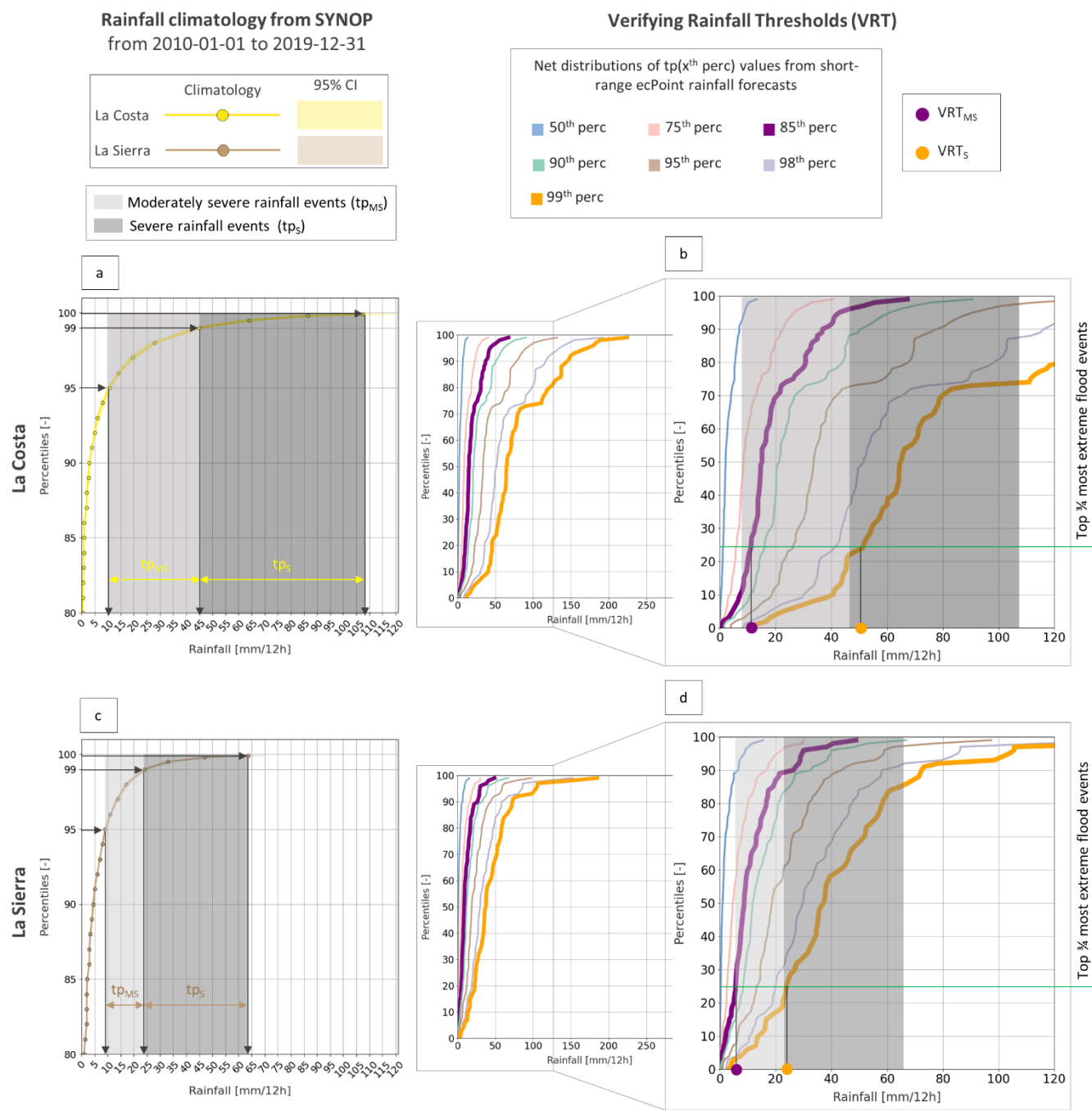


Figure 9 – Panels (a) and (c) show the rainfall climatologies from SYNOP observations, respectively, for “La Costa” and “La Sierra”, with 95% confidence intervals. The range of moderately severe (tp_{MS}) and severe rainfall totals (tp_S) are indicated, respectively, with a light and dark grey rectangle. Panels (b) and (d) show, respectively, the net distributions of flash-flood-triggering rainfall events (i.e., distribution in red in **Figure 8c) for “La Costa” and “La Sierra”, built from the rainfall totals corresponding to the 50th (in pale blue), 75th (in pale pink), 85th (in purple), 90th (in pale green), 95th (in pale brown), 98th (in grey), and 99th percentiles (in orange) in the distributions of short range ecPoint rainfall forecasts (i.e., the x^{th} percentile indicated in red in **Figure 8b**). The VRT_{MS} (purple circle) and VRT_S (orange circle) are defined using the net distribution that contains the cross point between the top ¼ most extreme flood events and the lower threshold of, respectively, the range of moderately severe and severe rainfall events.**

71

72

73

74

75

76

77

78

79

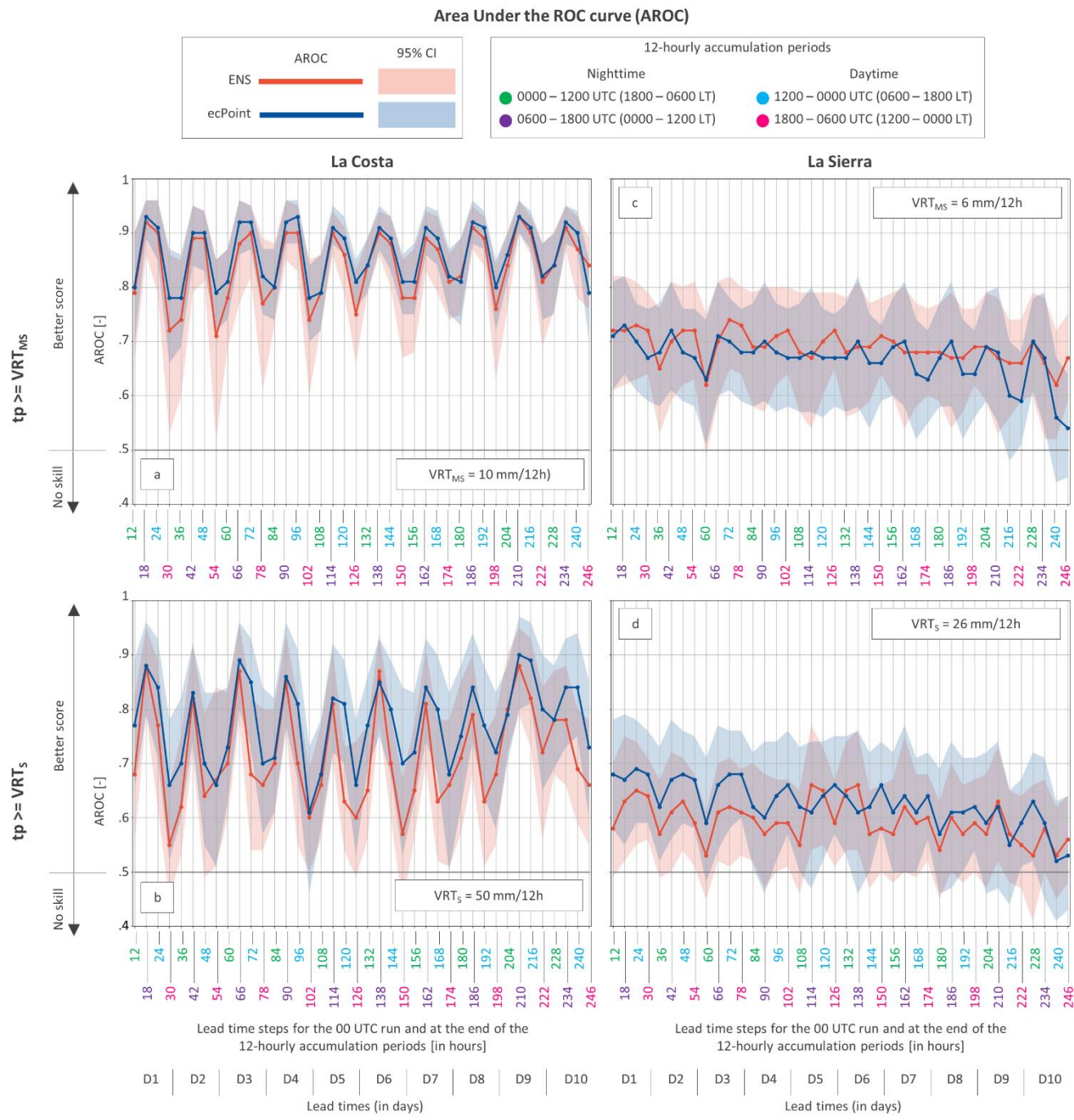
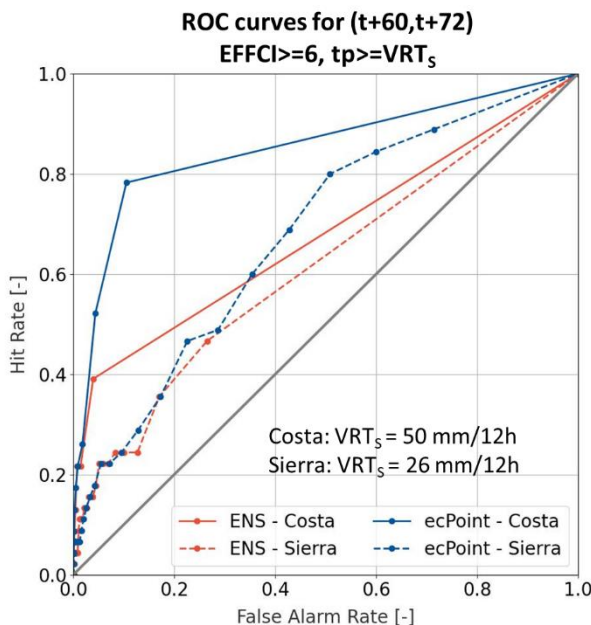


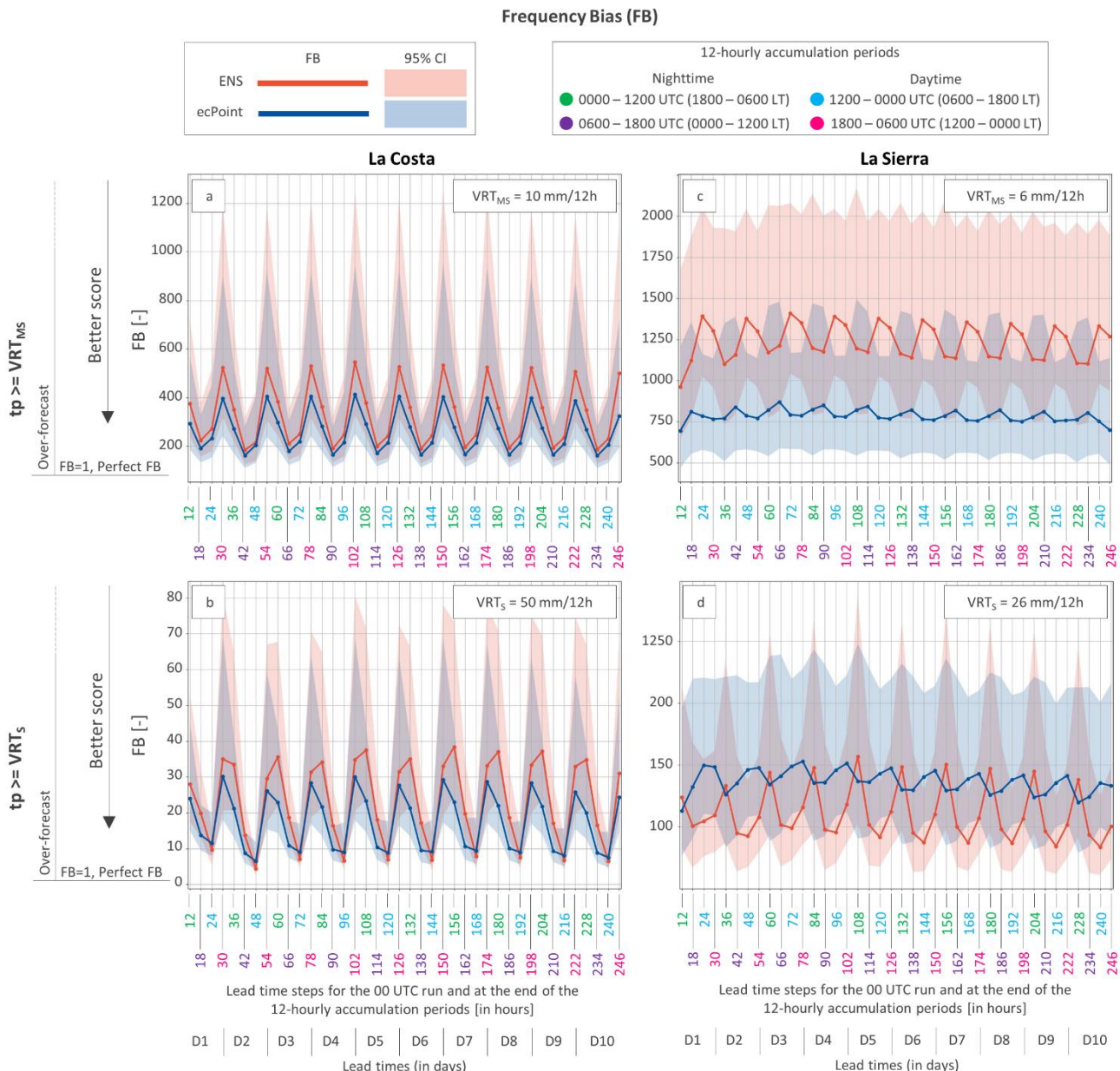
Figure 10 – Area under the ROC curve (AROC) for flood reports with $EFFCI \geq 6$. Panels (a) and (b) show the AROC, respectively, for $VRT_{MS} \geq 10 \text{ mm}/12\text{h}$ and $VRT_S \geq 50 \text{ mm}/12\text{h}$ in “La Costa”. Panels (c) and (d) show the AROC, respectively, for $VRT_{MS} \geq 6 \text{ mm}/12\text{h}$ and $VRT_S \geq 26 \text{ mm}/12\text{h}$ in “La Sierra”. The lines and the shaded areas represent, respectively, the values of the AROC and the confidence interval (CI) at 95% for ENS (in red) and ecPoint (in blue). The x-axis indicates the lead times steps for the 00 UTC run at the end of the 12-hourly accumulation period, expressed in hours. The colours associated with each step indicate the valid 12-hourly accumulation periods in UTC and local time (LT). The steps in green for 0000-1200 UTC (or 1800-0600 LT) and in purple for 0600-1800 UTC (or 0000-1200 LT) represent the 12-hourly accumulation periods during the nighttime. The steps in cyan for 1200-0000 UTC (or 0600-1800 LT) and in fuchsia for 1800-0600 UTC (or 1200-0000 LT) represent the 12-hourly accumulation periods during the daytime. Lead times are also expressed in days (from 1 to 10).



94

95 **Figure 11** – ROC curves built with flood reports with $\text{EFFCI} \geq 6$, for $\text{tp} \geq \text{VRT}_s$ and for the accumulation period between $(t+60, t+72)$, i.e., for 0600 to
96 1800 local time (LT). The red and the blue line denote, respectively, the ROC curves for ENS and ecPoint. The continuous and the dashed lines correspond
97 to the ROC curves for “La Costa” and “La Sierra”.

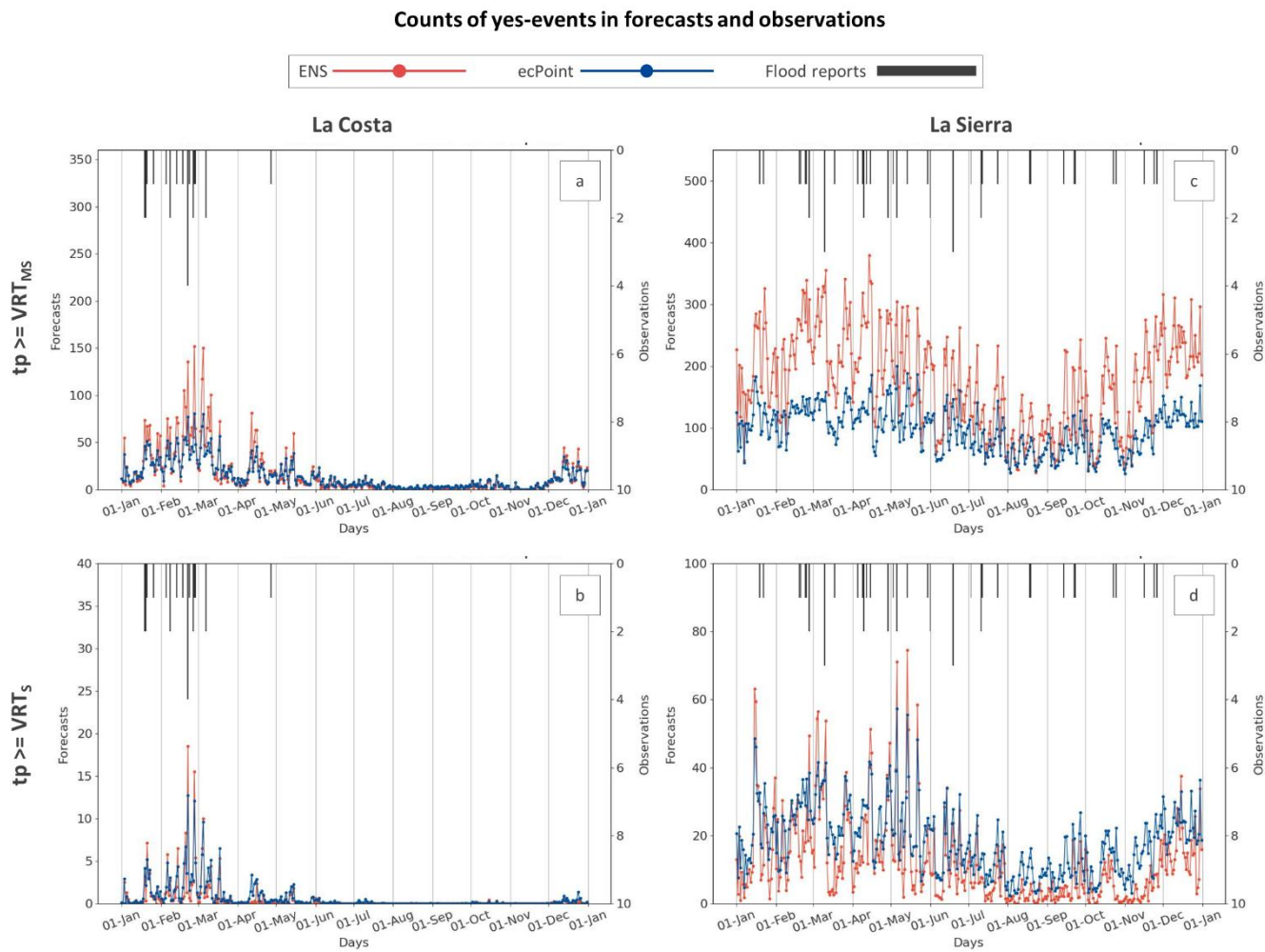
98

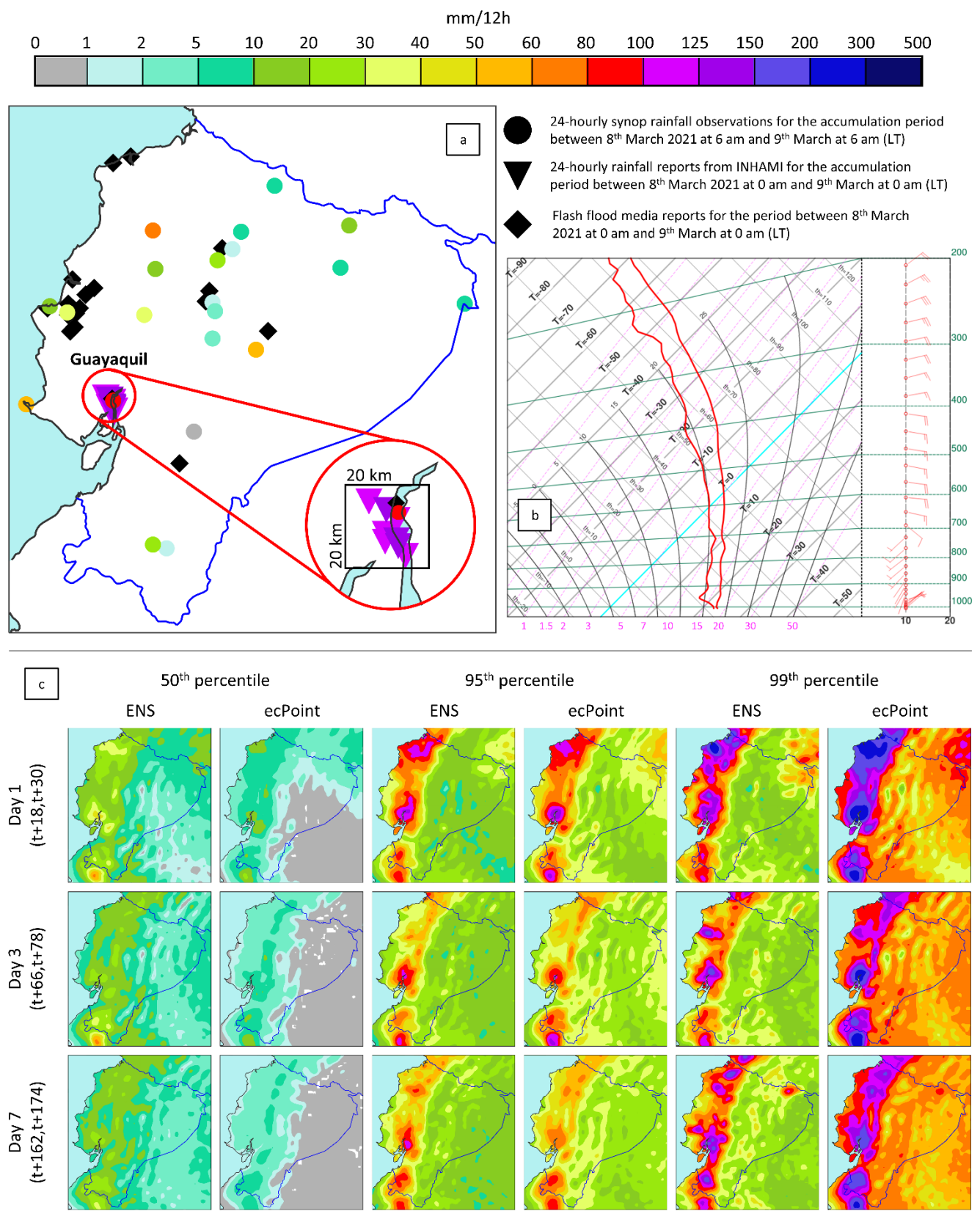


99

100
101
102
103
104
105
106
107

Figure 12 – Frequency bias (FB) for flood reports with $EFFCI \geq 6$. Panels (a) and (b) show the FB, respectively, for $VRT_{MS} \geq 10 \text{ mm/12h}$ and $VRT_S \geq 50 \text{ mm/12h}$ in “La Costa”. Panels (c) and (d) show the FB, respectively, for $VRT_{MS} \geq 6 \text{ mm/12h}$ and $VRT_S \geq 26 \text{ mm/12h}$ in “La Sierra”. The lines and the shaded areas represent, respectively, the values of the FB and the confidence interval (CI) at 95% for ENS (in red) and ecPoint (in blue). The x-axis indicates the valid 12-hourly accumulation periods in UTC and local time (LT). The steps in green for 0000-1200 UTC (or 1800-0600 LT) and in purple for 0600-1800 UTC (or 0000-1200 LT) represent the 12-hourly accumulation periods during the nighttime. The steps in cyan for 1200-0000 UTC (or 0600-1800 LT), and in fuchsia for 1800-0600 UTC (or 1200-0000 LT) represent the 12-hourly accumulation periods during the daytime. The lead times are also expressed in days (from 1 to 10).





115 **Figure 14** - Flash floods in Ecuador on 8th March 2021. Panel (a) shows 24-hourly synop rainfall observations between 8th March at 6 am and 9th March at 6 am (coloured dots), 24-hourly rainfall reports from INAMHI for Guayaquil between 8th March at 0 am and 9th March at 0 am (coloured triangles), and flash flood reports in different regions between 8th March at 0 am and 9th March at 0 am (black diamonds). Panel (b) shows the sounding for Guayaquil (lat: -2.2; lon: -79.9) valid for 8th March 2021 at 6 am. Panel (c) shows day 1, 3, and 7 forecasts from 00 UTC runs for ENS and ecPoint, valid for the accumulation period between 8th March at 12 am and 9th March at 0 am (when the rainfall event was at its peak). All reported times are meant to be in LT.

116

117

118

119

120

114

121 **Acknowledgments.**

122

123 **Data and software availability.** The data is available under request to the correspondent author. The software is available
124 in the following GitHub repository::

125

126 **Author contributions.** FMP contributed to the design and the implementation of the research, and to the analysis of the results.
127 HLC and CP supervised the project and helped built the manuscript structure. All authors contributed in the
128 discussion of the results and the writing of the manuscript.

129

130 **Conflict of interest.** We declare that there are no competing interests.

131

132 **Funding statement.** The study was supported by the Copernicus Emergency Management Service.

133 References

- 134 Adler, R. F., and Coauthors, 2018: The Global Precipitation Climatology Project (GPCP) Monthly Analysis (New Version 2.3)
135 and a Review of 2017 Global Precipitation. *Atmosphere (Basel)*, **9**, 138, <https://doi.org/10.3390/atmos9040138>.
- 136 Alfieri, L., and J. Thielen, 2015: A European precipitation index for extreme rain-storm and flash flood early warning.
137 *Meteorological Applications*, **22**, 3–13, <https://doi.org/10.1002/met.1328>.
- 138 Barrett, A. I., C. Wellmann, A. Seifert, C. Hoose, B. Vogel, and M. Kunz, 2019: One Step at a Time: How Model Time Step
139 Significantly Affects Convection-Permitting Simulations. *J Adv Model Earth Syst.*, **11**, 641–658,
140 <https://doi.org/10.1029/2018MS001418>.
- 141 Bazo, J., R. Singh, M. Destrooper, and E. C. De Perez, 2019: Pilot experiences in using seamless forecasts for early action:
142 The “ready-set-go!” approach in the red cross. *Sub-seasonal to Seasonal Prediction: The Gap Between Weather and*
143 *Climate Forecasting*, 387–398.
- 144 Beck, H. E., E. F. Wood, M. Pan, C. K. Fisher, D. G. Miralles, A. I. J. M. Van Dijk, T. R. McVicar, and R. F. Adler, 2019: MSWep
145 v2 Global 3-hourly 0.1° precipitation: Methodology and quantitative assessment. *Bull Am Meteorol Soc*, **100**, 473–
146 500, <https://doi.org/10.1175/BAMS-D-17-0138.1>.
- 147 Bendix, J., R. Rollenbeck, and C. Reudenbach, 2006: Diurnal patterns of rainfall in a tropical Andean valley of southern
148 Ecuador as seen by a vertically pointing K-band Doppler radar. *International Journal of Climatology*, **26**, 829–846,
149 <https://doi.org/10.1002/JOC.1267>.
- 150 Bischiniotis, K., B. van den Hurk, E. Coughlan de Perez, T. Veldkamp, G. G. Nobre, and J. Aerts, 2019: Assessing time, cost
151 and quality trade-offs in forecast-based action for floods. *International Journal of Disaster Risk Reduction*, **40**, 101252,
152 <https://doi.org/10.1016/j.ijdrr.2019.101252>.
- 153 Borga, M., M. Stoffel, L. Marchi, F. Marra, and M. Jakob, 2014: Hydrogeomorphic response to extreme rainfall in headwater
154 systems: Flash floods and debris flows. *J Hydrol (Amst)*, **518**, 194–205,
155 <https://doi.org/10.1016/J.JHYDROL.2014.05.022>.
- 156 Ben Bouallègue, Z., and D. S. Richardson, 2022: On the ROC area of ensemble forecasts for rare events. *Weather Forecast*,
157 **37**, 787–796, <https://doi.org/10.1175/waf-d-21-0195.1>.
- 158 Bucherie, A., F. Ayala, and A. Kruckiewicz, 2021: Ecuador historical flood occurrences and impacts dataset with Flash Flood
159 Confidence Index (2007–2020). *Zenodo*, <https://doi.org/10.5281/zenodo.4662886>.
- 160 ——, C. Hultquist, S. Adamo, C. Neely, F. Ayala, J. Bazo, and A. Kruckiewicz, 2022a: A comparison of social vulnerability
161 indices specific to flooding in Ecuador: principal component analysis (PCA) and expert knowledge. *International*
162 *Journal of Disaster Risk Reduction*, **73**, 102897, <https://doi.org/10.1016/j.ijdrr.2022.102897>.
- 163 ——, M. Werner, M. Van Den Homberg, and S. Tembo, 2022b: Flash flood warnings in context: Combining local knowledge
164 and large-scale hydro-meteorological patterns. *Natural Hazards and Earth System Sciences*, **22**, 461–480,
165 <https://doi.org/10.5194/nhess-22-461-2022>.
- 166 Buizza, R., 2019: Introduction to the special issue on “25 years of ensemble forecasting.” *Quarterly Journal of the Royal*
167 *Meteorological Society*, **145**, 1–11, <https://doi.org/10.1002/qj.3370>.
- 168 Buytaert, W., R. Celleri, P. Willems, B. De Bièvre, and G. Wyseure, 2006: Spatial and temporal rainfall variability in
169 mountainous areas: A case study from the south Ecuadorian Andes. *J Hydrol (Amst)*, **329**, 413–421,
170 <https://doi.org/10.1016/J.JHYDROL.2006.02.031>.
- 171 Corral, C., M. Berenguer, D. Sempere-Torres, L. Poletti, F. Silvestro, and N. Rebora, 2019: Comparison of two early warning
172 systems for regional flash flood hazard forecasting. *J Hydrol (Amst)*, **572**, 603–619,
173 <https://doi.org/10.1016/j.jhydrol.2019.03.026>.
- 174 Coughlan de Perez, E., and Coauthors, 2022: Adapting to climate change through anticipatory action: The potential use of
175 weather-based early warnings. *Weather Clim Extrem*, **38**, 100508, <https://doi.org/10.1016/j.wace.2022.100508>.
- 176 Davolio, S., F. Silvestro, and T. Gastaldo, 2017: Impact of rainfall assimilation on high-resolution hydrometeorological
177 forecasts over Liguria, Italy. *J Hydrometeorol*, **18**, 2659–2680, <https://doi.org/10.1175/JHM-D-17-0073.1>.
- 178 Demissie, B., and Coauthors, 2021: Flood hazard in a semi-closed basin in northern Ethiopia: Impact and resilience. *Geo*, **8**,
179 e00100, <https://doi.org/10.1002/GEO2.100>.
- 180 DiCiccio, T. J., and B. Efron, 1996: Bootstrap confidence intervals. *Statistical Science*, **11**, 189–212,
181 <https://doi.org/10.1214/ss/1032280214>.
- 182 Dinis, P. A., J. Huvi, M. C. Pinto, and J. Carvalho, 2021: Disastrous Flash Floods Triggered by Moderate to Minor Rainfall
183 Events. Recent Cases in Coastal Benguela (Angola). *Hydrology* 2021, Vol. 8, Page 73, **8**, 73,
184 <https://doi.org/10.3390/HYDROLOGY8020073>.

- 185 Dordevic, M., P. Mutic, and H. Kim, 2020: Flash Flood Guidance System: Response to one of the deadliest hazards. *WMO*
186 *Bulletin*, **69**, 29–33.
- 187 Douinot, A., H. Roux, P. A. Garambois, K. Larnier, D. Labat, and D. Dartus, 2016: Accounting for rainfall systematic spatial
188 variability in flash flood forecasting. *J Hydrol (Amst)*, **541**, 359–370, <https://doi.org/10.1016/J.JHYDROL.2015.08.024>.
- 189 Emerton, R. E., and Coauthors, 2016: Continental and global scale flood forecasting systems. *Wiley Interdisciplinary Reviews:*
190 *Water*, **3**, 391–418, [https://doi.org/https://doi.org/10.1002/wat2.1137](https://doi.org/10.1002/wat2.1137).
- 191 Galarza-Villamar, J. A., C. Leeuwis, G. M. Pila-Quinga, F. Cecchi, and C. M. Párraga-Lema, 2018: Local understanding of
192 disaster risk and livelihood resilience: The case of rice smallholders and floods in Ecuador. *International Journal of*
193 *Disaster Risk Reduction*, **31**, 1107–1120, <https://doi.org/10.1016/j.ijdrr.2018.08.009>.
- 194 Gascón, E., A. Montani, and T. D. Hewson, 2023: Post-processing output from ensembles with and without parametrised
195 convection, to create accurate, blended, high-fidelity rainfall forecasts. <https://doi.org/10.48550/arxiv.2301.04485>.
- 196 Gaume, E., and Coauthors, 2009: A compilation of data on European flash floods. *J Hydrol (Amst)*, **367**, 70–78,
197 <https://doi.org/10.1016/j.jhydrol.2008.12.028>.
- 198 Georgakakos, K. P., and Coauthors, 2021: The Flash Flood Guidance System Implementation Worldwide: A Successful
199 Multidecadal Research-To-Operations Effort. *Bull Am Meteorol Soc*, **1**, 1–35, <https://doi.org/10.1175/bams-d-20-0241.1>.
- 200 Gourley, J. J., and Coauthors, 2017: The FLASH Project - Improving the Tools for Flash Flood Monitoring and Prediction
201 across the United States. *Bull Am Meteorol Soc*, **98**, 361–372, <https://doi.org/https://doi.org/10.1175/BAMS-D-15-00247.1>.
- 202 Haiden, T., and S. Duffy, 2016: Use of high-density observations in precipitation verification. *ECMWF Newsletter*, 20–25,
203 <https://doi.org/10.21957/hsacrdem>.
- 204 Haiden, T., M. Janousek, F. Vitart, Z. Ben-Boualleugue, L. Ferranti, F. Prates, and D. Richardson, 2021: Evaluation of
205 ECMWF forecast, including 2021 upgrade. *ECMWF technical memoranda*, **56**, <https://doi.org/10.21957/90pgicjk4>.
- 206 Haiden, T., M. Janousek, F. Vitart, Z. Ben-Boualleugue, and F. Prates, 2023: Evaluation of ECMWF forecasts, including the
207 2023 upgrade. *ECMWF Technical Memoranda*, **911**, 1–60.
- 208 Hamill, T. M., J. S. Whitaker, and S. L. Mullen, 2006: Reforecasts: An important dataset for improving weather predictions.
209 *Bull Am Meteorol Soc*, **87**, 33–46, <https://doi.org/10.1175/BAMS-87-1-33>.
- 210 Hemri, S., T. Hewson, E. Gascon, J. Rajczak, J. Bhend, C. Spririg, L. Moret, and M. Liniger, 2022: How do ecPoint precipitation
211 forecasts compare with postprocessed multi-model ensemble predictions over Switzerland? *ECMWF Technical*
212 *Memorandum*, **901**.
- 213 Hersbach, H., and Coauthors, 2020: The ERA5 global reanalysis. *Quarterly Journal of the Royal Meteorological Society*, **146**,
214 1999–2049, <https://doi.org/10.1002/qj.3803>.
- 215 Hewson, T., F. Pillosu, E. Gascòn, and M. Vučović, 2023: Post-processing ERA5 output with ecPoint. *ECMWF Newsletter*,.
- 216 Hewson, T. D., and F. M. Pillosu, 2021: A low-cost post-processing technique improves weather forecasts around the world.
217 *Commun Earth Environ*, **2**, <https://doi.org/10.1038/s43247-021-00185-9>.
- 218 Hirabayashi, Y., M. Tanoue, O. Sasaki, X. Zhou, and D. Yamazaki, 2021: Global exposure to flooding from the new CMIP6
219 climate model projections. *Sci Rep*, **11**, 1–7, <https://doi.org/10.1038/s41598-021-83279-w>.
- 220 Hitchens, N. M., H. E. Brooks, and M. P. Kay, 2013: Objective limits on forecasting skill of rare events. *Weather Forecast*, **28**,
221 525–534, <https://doi.org/10.1175/WAF-D-12-00113.1>.
- 222 Hurford, A. P., S. J. Priest, D. J. Parker, and D. M. Lumbroso, 2012: The effectiveness of extreme rainfall alerts in predicting
223 surface water flooding in England and Wales. *International Journal of Climatology*, **32**, 1768–1774,
224 <https://doi.org/https://doi.org/10.1002/joc.2391>.
- 225 Ibarreche, J., and Coauthors, 2020: Flash flood early warning system in Colima, Mexico. *Sensors (Switzerland)*, **20**, 1–26,
226 <https://doi.org/10.3390/s20185231>.
- 227 Ilbay-Yupa, M., W. Lavado-Casimiro, P. Rau, R. Zubíeta, and F. Castillón, 2021: Updating regionalization of precipitation in
228 Ecuador. *Theor Appl Climatol*, **143**, 1513–1528, <https://doi.org/10.1007/S00704-020-03476-X/FIGURES/7>.
- 229 Imhoff, R. O., C. C. Brauer, K. J. van Heeringen, R. Uijlenhoet, and A. H. Weerts, 2022: Large-Sample Evaluation of Radar
230 Rainfall Nowcasting for Flood Early Warning. *Water Resour Res*, **58**, e2021WR031591,
231 <https://doi.org/10.1029/2021WR031591>.
- 232 Javelle, P., C. Fouchier, P. Arnaud, and J. Lavabre, 2010: Flash flood warning at ungauged locations using radar rainfall and
233 antecedent soil moisture estimations. *J Hydrol (Amst)*, **394**, 267–274,
234 <https://doi.org/https://doi.org/10.1016/j.jhydrol.2010.03.032>.

- 237 ——, D. Organde, J. Demargne, C. Saint-Martin, C. De Saint-Aubin, L. Garandea, and B. Janet, 2016: Setting up a French
238 national flash flood warning system for ungauged catchments based on the AIGA method. *E3S Web of Conferences*,
239 Vol. 7 of, 718010–18010.
- 240 Jolliffe, I. T., and D. B. Stephenson, 2011: *Forecast Verification: A Practitioner's Guide in Atmospheric Science*. 2nd Editio.
241 John Wiley & Sons, Ltd.,
- 242 Jonkman, S. N., and J. K. Vrijling, 2008: Loss of life due to floods. *J Flood Risk Manag*, **1**, 43–56,
243 <https://doi.org/10.1111/j.1753-318x.2008.00006.x>.
- 244 Junquas, C., and Coauthors, 2022: Regional climate modeling of the diurnal cycle of precipitation and associated
245 atmospheric circulation patterns over an Andean glacier region (Antisana, Ecuador). *Clim Dyn*, **58**, 3075–3104,
246 <https://doi.org/10.1007/S00382-021-06079-Y/FIGURES/13>.
- 247 Kiptum, A., and Coauthors, 2023: Advancing operational flood forecasting, early warning and risk management with new
248 emerging science: Gaps, opportunities and barriers in Kenya. *Journal of Flood Risk Management*, John Wiley & Sons,
249 Ltd, e12884.
- 250 Kruczakiewicz, A., A. Bucherie, F. Ayala, and J. Bazo, 2021a: Forecast-based financing for flash floods: a flash flood confidence
251 index to improve flood reporting. *Anticipation Hub*, [https://www.anticipation-hub.org/news/forecast-based-](https://www.anticipation-hub.org/news/forecast-based-financing-for-flash-floods-a-flash-flood-confidence-index)
252 [financing-for-flash-floods-a-flash-flood-confidence-index](https://doi.org/10.3390/rs13142764).
- 253 ——, ——, ——, C. Hultquist, H. Vergara, S. Mason, J. Bazo, and A. de Sherbinin, 2021b: Development of a flash flood
254 confidence index from disaster reports and geophysical susceptibility. *Remote Sens (Basel)*, **13**, 2764,
255 <https://doi.org/10.3390/rs13142764>.
- 256 Laraque, A., and Coauthors, 2009: Sediment budget of the Napo River, Amazon Basin, Ecuador and Peru. *Hydrol Process*,
257 **23**, 3509–3524, <https://doi.org/10.1002/hyp.7463>.
- 258 Lavers, D. A., S. Harrigan, and C. Prudhomme, 2021: Precipitation Biases in the ECMWF Integrated Forecasting System. *J*
259 *Hydrometeorol*, <https://doi.org/10.1175/jhm-d-20-0308.1>.
- 260 Liu, C., L. Guo, L. Ye, S. Zhang, Y. Zhao, and T. Song, 2018: A review of advances in China's flash flood early-warning system.
261 *Natural Hazards*, **92**, 619–634, <https://doi.org/10.1007/s11069-018-3173-7>.
- 262 Lowrie, C., A. Kruczakiewicz, S. N. McClain, M. Nielsen, and S. J. Mason, 2022: Evaluating the usefulness of VGI from Waze
263 for the reporting of flash floods. *Scientific Reports* 2022 12:1, **12**, 1–13, <https://doi.org/10.1038/s41598-022-08751-7>.
- 264 Luong, T. T., J. Pöschmann, R. Kronenberg, and C. Bernhofer, 2021: Rainfall threshold for flash flood warning based on
265 model output of soil moisture: Case study wernersbach, germany. *Water (Switzerland)*, **13**, 1–15,
266 <https://doi.org/10.3390/w13081061>.
- 267 Ma, M., and Coauthors, 2021: Development of a new rainfall-triggering index of flash flood warning-case study in Yunnan
268 province, China. *J Flood Risk Manag*, **14**, 1–9, <https://doi.org/10.1111/jfr3.12676>.
- 269 Marsigli, C., and Coauthors, 2021: Review article: Observations for high-impact weather and their use in verification. *Natural*
270 *Hazards and Earth System Sciences*, **21**, 1297–1312, <https://doi.org/10.5194/NHESS-21-1297-2021>.
- 271 Mitheu, F., E. Tarnavsky, A. Ficchì, E. Stephens, R. Cornforth, and C. Petty, 2023: The utility of impact data in flood forecast
272 verification for anticipatory actions: Case studies from Uganda and Kenya. *J Flood Risk Manag*, e12911,
273 <https://doi.org/10.1111/JFR3.12911>.
- 274 Norbiato, D., M. Borga, S. Degli Esposti, E. Gaume, and S. Anquetin, 2008: Flash flood warning based on rainfall thresholds
275 and soil moisture conditions: An assessment for gauged and ungauged basins. *J Hydrol (Amst)*, **362**, 274–290,
276 <https://doi.org/10.1016/j.jhydrol.2008.08.023>.
- 277 Papagiannaki, K., K. Lagouvardos, V. Kotroni, and A. Bezes, 2015: Flash flood occurrence and relation to the rainfall hazard
278 in a highly urbanized area. *Natural Hazards and Earth System Sciences*, **15**, 1859–1871,
279 <https://doi.org/10.5194/nhess-15-1859-2015>.
- 280 De Perez, E. C., and Coauthors, 2016: Action-based flood forecasting for triggering humanitarian action. *Hydrol Earth Syst*
281 *Sci*, **20**, 3549–3560, <https://doi.org/https://doi.org/10.5194/hess-20-3549-2016>.
- 282 Pinos, J., and L. Timbe, 2020: Mountain Riverine Floods in Ecuador: Issues, Challenges, and Opportunities. *Frontiers in*
283 *Water*, **2**, 36, <https://doi.org/10.3389/frwa.2020.545880>.
- 284 ——, and A. Quesada-Román, 2022: Flood risk-related research trends in Latin America and the Caribbean. *Water*
285 (*Switzerland*), **14**, 10, <https://doi.org/10.3390/w14010010>.
- 286 Ramos Filho, G. M., V. H. R. Coelho, E. da S. Freitas, Y. Xuan, and C. das N. Almeida, 2021: An improved rainfall-threshold
287 approach for robust prediction and warning of flood and flash flood hazards. *Natural Hazards*, **105**, 2409–2429,
288 <https://doi.org/10.1007/s11069-020-04405-x>.

- 290 Raynaud, D., J. Thielen, P. Salamon, P. Burek, S. Anquetin, and L. Alfieri, 2015: A dynamic runoff co-efficient to improve flash
291 flood early warning in Europe: Evaluation on the 2013 central European floods in Germany. *Meteorological*
292 *Applications*, **22**, 410–418, <https://doi.org/10.1002/met.1469>.
- 293 Recalde-Coronel, C. G., A. G. Barnston, and Á. G. Muñoz, 2014: Predictability of december-april rainfall in coastal and
294 Andean Ecuador. *J Appl Meteorol Climatol*, **53**, 1471–1493, <https://doi.org/10.1175/JAMC-D-13-0133.1>.
- 295 Recalde-Coronel, G. C., B. Zaitchik, and W. K. Pan, 2020: Madden–Julian oscillation influence on sub-seasonal rainfall
296 variability on the west of South America. *Clim Dyn*, **54**, 2167–2185, <https://doi.org/10.1007/s00382-019-05107-2>.
- 297 Robbins, J. C., and H. A. Titley, 2018: Evaluating high-impact precipitation forecasts from the Met Office Global Hazard Map
298 (GHM) using a global impact database. *Meteorological Applications*, **25**, 548–560,
299 <https://doi.org/https://doi.org/10.1002/met.1720>.
- 300 Šakić Trogrić, R., M. van den Homberg, M. Budimir, C. McQuistan, A. Sneddon, and B. Golding, 2022: Early Warning Systems
301 and Their Role in Disaster Risk Reduction. *Towards the “Perfect” Weather Warning*, 11–46.
- 302 Shuvo, S. D., T. Rashid, S. K. Panda, S. Das, and D. A. Quadir, 2021: Forecasting of pre-monsoon flash flood events in the
303 northeastern Bangladesh using coupled hydrometeorological NWP modelling system. *Meteorology and Atmospheric*
304 *Physics*, 1–23, <https://doi.org/10.1007/s00703-021-00831-z>.
- 305 Song, H. J., B. Lim, and S. Joo, 2019: Evaluation of rainfall forecasts with heavy rain types in the high-resolution unified
306 model over South Korea. *Weather Forecast*, **34**, 1277–1293, <https://doi.org/10.1175/WAF-D-18-0140.1>.
- 307 Speight, L., and Coauthors, 2018: Developing surface water flood forecasting capabilities in Scotland: an operational pilot
308 for the 2014 Commonwealth Games in Glasgow. *J Flood Risk Manag*, **11**, S884–S901,
309 <https://doi.org/10.1111/jfr3.12281>.
- 310 Speight, L. J., M. D. Cranston, C. J. White, and L. Kelly, 2021: Operational and emerging capabilities for surface water flood
311 forecasting. *Wiley Interdisciplinary Reviews: Water*, **8**, <https://doi.org/10.1002/wat2.1517>.
- 312 Tapiador, F. J., R. Roca, A. Del Genio, B. Dewitt, W. Petersen, and F. Zhang, 2019: Is precipitation a good metric for model
313 performance? *Bull Am Meteorol Soc*, **100**, 223–233, <https://doi.org/10.1175/BAMS-D-17-0218.1>.
- 314 Tobar, V., and G. Wyseure, 2018: Seasonal rainfall patterns classification, relationship to ENSO and rainfall trends in
315 Ecuador. *International Journal of Climatology*, **38**, 1808–1819, <https://doi.org/10.1002/joc.5297>.
- 316 Trigg, M. A., M. D. Wilson, P. D. Bates, M. S. Horritt, D. E. Alsdorf, B. R. Forsberg, and M. C. Vega, 2009: Amazon flood wave
317 hydraulics. *J Hydrol (Amst)*, **374**, 92–105, <https://doi.org/10.1016/j.jhydrol.2009.06.004>.
- 318 UNDRR, 2021: Desinventar Project. *Plataforma Desinventar Sendai*,. <https://db.desinventar.org/>.
- 319 Vuille, M., R. S. Bradley, and F. Keimig, 2000: Climate variability in the Andes of Ecuador and its relation to tropical Pacific
320 and Atlantic Sea Surface temperature anomalies. *J Clim*, **13**, 2520–2535, [https://doi.org/10.1175/1520-0442\(2000\)013<2520:CVITAO>2.0.CO;2](https://doi.org/10.1175/1520-0442(2000)013<2520:CVITAO>2.0.CO;2).
- 321 Wen, Y., T. Schuur, H. Vergara, and C. Kuster, 2021: Effect of Precipitation Sampling Error on Flash Flood Monitoring and
322 Prediction: Anticipating Operational Rapid-Update Polarimetric Weather Radars. *J Hydrometeorol*, **22**, 1913–1929,
323 <https://doi.org/10.1175/JHM-D-19-0286.1>.
- 324 Wheeler, M. C., and H. H. Hendon, 2004: An all-season real-time multivariate MJO index: Development of an index for
325 monitoring and prediction. *Mon Weather Rev*, **132**, 1917–1932, [https://doi.org/10.1175/1520-0493\(2004\)132<1917:AARMMI>2.0.CO;2](https://doi.org/10.1175/1520-0493(2004)132<1917:AARMMI>2.0.CO;2).
- 326 Xing, Y., Q. Liang, G. Wang, X. Ming, and X. Xia, 2019: City-scale hydrodynamic modelling of urban flash floods: the issues
327 of scale and resolution. *Natural Hazards*, **96**, 473–496, <https://doi.org/10.1007/s11069-018-3553-z>.
- 328 Zanchetta, A. D. L., and P. Coulibaly, 2020: Recent advances in real-time pluvial flash flood forecasting. *Water (Switzerland)*,
329 **12**, 570, <https://doi.org/10.3390/w12020570>.
- 330 —, —, and V. Fortin, 2022: Forecasting High-Flow Discharges in a Flashy Catchment Using Multiple Precipitation
331 Estimates as Predictors in Machine Learning Models. *Hydrology*, **9**, 216, <https://doi.org/10.3390/hydrology9120216>.
- 332 Zeman, C., N. P. Wedi, P. D. Dueben, N. Ban, and C. Schär, 2021: Model intercomparison of COSMO 5.0 and IFS 45r1 at
333 kilometer-scale grid spacing. *Geosci Model Dev*, **14**, 4617–4639, <https://doi.org/10.5194/gmd-14-4617-2021>.
- 334
- 335
- 336